

Tsunami Induced by the Strike-Slip Fault of the 2018 Palu Earthquake (Mw=7.5), Sulawesi Island, Indonesia

Tung-Cheng Ho¹, Kenji Satake¹, Shingo Watada¹, Ming-Che Hsieh², RAY Y. CHUANG³, Yosuke Aoki¹, Iyan Eka Mulia¹, Aditya Riadi Gusman⁴, and Chih-Heng Lu⁵

¹University of Tokyo

²Sinotech Engineering Consultants, Inc.

³National Taiwan University, Indiana University

⁴GNS

⁵National Taiwan University

November 23, 2022

Abstract

An unusual devastating tsunami occurred on 28 September 2018 after a strike-slip faulting earthquake in Sulawesi, Indonesia. The induced tsunami struck Palu city with 4-m wave height and flow depth. We performed a two-step analysis to investigate the source of the tsunami. We first conducted the teleseismic source inversion and obtained the slip distribution of the strike-slip fault. Our tsunami simulation from the coseismic deformation of the seismically-estimated strike-slip faulting produced a tsunami comparable to the leading part of the observation at Pantoloan. We then jointly utilized the tsunami waveform and Synthetic Aperture Radar (SAR) data to reconstruct the detailed slip distribution on the fault plane. Because of the lack of SAR data in the bay, the tsunami data is necessary to constrain the offshore slip distribution, which directly induces the tsunami. The inverted source model shows a strike-slip fault which consists of three segments extending from the epicenter to the south of 1.4°S with two bends and two asperities around Palu city. The joint inversion model accurately reconstructs the observed surface displacements and the leading part of the tsunami waveform. Our result exhibits the significant contribution of the strike-slip faulting to the tsunami, but it also suggests additional tsunami sources, such as landslides, for the high inundations near Palu bay. The result also indicates that regional devastating tsunamis can result from an onshore strike-slip fault with localized large dip slip.

1 **Tsunami Induced by the Strike-Slip Fault of the 2018 Palu Earthquake (Mw=7.5),**
2 **Sulawesi Island, Indonesia**

3
4 **Tung-Cheng Ho^{1*}, Kenji Satake¹, Shingo Watada¹, Ming-Che Hsieh², Ray Y. Chuang³,**
5 **Yosuke Aoki¹, Iyan E. Mulia¹, Aditya Riadi Gusman⁴, Chih-Heng Lu³**

6
7 ¹Earthquake Research Institute, the University of Tokyo, Tokyo, Japan.

8 ²Disaster Prevention Technology Research Center, Sinotech Engineering Consultants, Taipei,
9 Taiwan.

10 ³Department of Geography, National Taiwan University, Taipei, Taiwan.

11 ⁴GNS Science, Lower Hutt, New Zealand.

12
13 Corresponding author: Tung-Cheng Ho (dong@eri.u-tokyo.ac.jp)

14 *Now at Disaster Prevention Research Institute (DPRI), Kyoto University.

15
16 **Key Points:**

- 17 • The two-step analysis of teleseismic, SAR, and tsunami data retrieves an earthquake
18 source model that explains the observed tsunami.
- 19 • A strike-slip fault with localized large dip slip of the 2018 Palu earthquake induced
20 the devastating regional tsunami.
- 21 • Onshore strike-slip faults should also be regarded as a potential source of tsunami for
22 regional areas.

23
24 **Abstract**

25 An unusual devastating tsunami occurred on 28 September 2018 after a strike-slip faulting
26 earthquake in Sulawesi, Indonesia. The induced tsunami struck Palu city with 4-m wave
27 height and flow depth. We performed a two-step analysis to investigate the source of the
28 tsunami. We first conducted the teleseismic source inversion and obtained the slip
29 distribution of the strike-slip fault. Our tsunami simulation from the coseismic deformation of
30 the seismically-estimated strike-slip faulting produced a tsunami comparable to the leading
31 part of the observation at Pantoloan. We then jointly utilized the tsunami waveform and
32 Synthetic Aperture Radar (SAR) data to reconstruct the detailed slip distribution on the fault
33 plane. Because of the lack of SAR data in the bay, the tsunami data is necessary to constrain
34 the offshore slip distribution, which directly induces the tsunami. The inverted source model
35 shows a strike-slip fault which consists of three segments extending from the epicenter to the
36 south of 1.4°S with two bends and two asperities around Palu city. The joint inversion model
37 accurately reconstructs the observed surface displacements and the leading part of the

38 tsunami waveform. Our result exhibits the significant contribution of the strike-slip faulting
39 to the tsunami, but it also suggests additional tsunami sources, such as landslides, for the high
40 inundations near Palu bay. The result also indicates that regional devastating tsunamis can
41 result from an onshore strike-slip fault with localized large dip slip.

42 **Plain Language Summary**

43 The Palu, Indonesia, earthquake of 28 September 2018 produced tsunami flooding and
44 damage in Palu city. Because of its strike-slip mechanism, which is not efficient to produce
45 tsunamis, multiple submarine landslides have been speculated as a tsunami source. We found
46 that the fault model estimated by teleseismic waves (recorded globally outside Indonesia) can
47 reproduce the tsunami recorded at the Pantoloan station in Palu bay. This indicates that the
48 source of tsunami recorded at Pantoloan is mostly the fault motion accompanied by the
49 earthquake. We then combined the displacements measured by Synthetic Aperture Radar
50 images and the Pantoloan tsunami waveform to estimate the slip distribution on the fault. The
51 slip model shows a strike-slip fault with two large slip areas located near Palu city between
52 two bends. This model well reproduces the Pantoloan tsunami but fails to fully reproduce the
53 inundations in Palu city, suggesting that additional tsunami sources, such as landslides,
54 should be responsible for the large inundations in Palu city. Our result suggests that a strike-
55 slip fault can induce a devastating local tsunami.

56 **1 Introduction**

57 On September 28, 2018, a devastating tsunami impacted Palu city, Sulawesi Island,
58 Indonesia (Figure 1) after an M7.5 earthquake. A moment tensor solution obtained by the
59 U.S. Geological Survey (USGS) from W phase waveforms suggests strike-slip faulting with a
60 high dip angle ($\sim 67^\circ$) at a shallow depth (~ 13 km). The estimated nodal plane strikes
61 approximately north-south (N10°W) with a rake angle of -17° , implying the presence of some
62 normal faulting component.

63 The Palu-Koro fault (Figure 1), the plate boundary between the Makassar block and
64 the North Sula block, is thought to be responsible for the Palu earthquake. Global Navigation
65 Satellite System (GNSS) monitoring shows that the relative velocity on the Palu-Koro fault
66 zone accommodates 42 mm/yr of a complex transtensive motion with a 39 mm/yr of strike-
67 slip and 11-14 mm/yr of extension (Socquet et al., 2006). Three tsunami events associated
68 with the Palu-Koro fault zone have been reported in 1927, 1968, and 1996, of which the 1927
69 and 1968 earthquakes also caused destructive tsunamis in Palu bay (Prasetya et al., 2001).
70 Socquet et al. (2019) and Bao et al. (2019) pointed out that the 2018 earthquake might have
71 ruptured with a supershear velocity from the back-projection of the seismic wavefield and the
72 geodetic data.

73 A slip distribution obtained by USGS from teleseismic waveforms (United States
74 Geological Survey, 2018) suggests an asperity with a maximum of more than 8 m slip under
75 Palu bay. The source time function shows that most of the moment was released within 30 s
76 after the earthquake origin time. Socquet et al. (2019) utilized horizontal offsets in SAR
77 images to estimate the slip distribution and indicated a peak slip of more than 5 m of strike-
78 slip and 2 m of reverse faulting dip-slip near the asperity.

79 Devastating tsunami inundations impacted the areas around Palu bay after the
80 earthquake. High runups were measured by field surveys (Muhari et al., 2018; Omira et al.,
81 2019; Yalciner et al., 2018; Paulik et al., 2019; Mikami et al., 2019). Flow depths of up to 5
82 m on the south coast of Palu bay (Palu City), up to 2 m observed on the east coast, and higher
83 than 1 m on the west coast were observed. The tsunami waveform was recorded in the bay by

84 a tide gauge at the port of Pantoloan (Figure 1). The other tide gauge located ~200 km outside
85 of the bay at Mamuju recorded tsunami waves from about 20 minutes after the earthquake
86 origin time. However, numerical simulations showed that the tsunami waves take at least 40
87 minutes from the source area to the Mamuju station (Heidarzadeh et al., 2019). Therefore, the
88 tsunami recorded at the Mamuju station is not considered to be directly originated from the
89 earthquake.

90 Sassa and Takagawa (2019) indicated that the earthquake caused extensive
91 liquefaction which induced liquefied sediment flows in the coastal area, resulting in the
92 devastating tsunami. Heidarzadeh et al. (2019) performed tsunami simulation using the
93 source model of USGS (United States Geological Survey, 2018). They fairly well
94 reconstructed the tsunami waveform at Pantoloan although the wave height was slightly
95 underestimated. They mentioned that a large submarine landslide may intensify the tsunami.
96 Gusman et al. (2019) focused on the vertical displacements around the narrow bay that
97 generated the tsunami. They concluded that the tsunami inundation was caused by a
98 combination of the earthquake faulting, landslides, and the high tide time of the event.

99 Ulrich et al. (2019) used a physics-based, coupled earthquake-tsunami model to
100 demonstrate that the tsunami wave and inundations were mainly generated by the earthquake
101 deformation and suggested that landslide may not be the primary source of the tsunami. Fang
102 et al. (2019) investigated the source geometry and rupture using the SAR interferometry
103 (InSAR) of ALOS-2 images and regional broadband seismograms. Their rupture model
104 shows a rupture propagated mainly southward and a major asperity located at the south of
105 Palu bay with a maximum slip of 6.5 m. They concluded that the offshore asperities with
106 significant normal-slip components are responsible for the tsunami.

107 Yolsal-Çevikbilen et al. (2019) inverted the teleseismic waveforms to estimate the slip
108 distribution. Their model shows an asperity concentrated in the bay area, and they suggested
109 that the normal faulting could be partially responsible for the tsunami in Palu bay. However,
110 Lee et al. (2019) expected a smaller tsunami than the observation from their inversion of
111 teleseismic waveforms. Besides coseismic effects, they suggested that other sources, such as
112 a submarine landslide, are possible to account for the local tsunami.

113 The primary tsunami source is still controversial and the contribution of the
114 earthquake fault motion to the generation of tsunami is not well clarified, although strike-slip
115 faulting is generally considered not to generate a devastating tsunami. To better understand
116 the tsunami generation by a strike-slip fault, we performed a two-step analysis that utilized
117 teleseismic, SAR, and tsunami data to examine the contribution of the fault slip to the
118 tsunami generation and estimate the slip distribution on the fault plane.

119

120 **2 Data**

121 2.1 Teleseismic Body and Surface Waveforms

122 The teleseismic records from the Global Seismograph Network (GSN) which provides
123 good azimuthal coverage for inversion (Figure S1) were utilized to estimate the slip
124 distribution of the Palu earthquake. The passbands for the body and surface waves are 1-180 s
125 and 200-500 s, respectively.

126

127 2.2 Surface Displacements from SAR Data

128 Sub-pixel correlation of SAR intensity images before and after an earthquake provide
129 a high-resolution measurement of coseismic surface displacements (e.g., Michel et al., 1999).
130 The azimuth offsets, displacements in the azimuth direction, extracted from the Sentinel-1
131 satellite images exhibit clear displacement offsets, from which we can constrain the geometry
132 of the surface faulting.

133 In order to measure coseismic displacements, we used Sentinel-1 satellite images on 7
134 June 2018 and 5 October 2018 from the descending orbits, and on 13 March 2017 and 4
135 October 2018 from the ascending orbits. It is difficult to generate interferograms with C-band
136 images due to temporal decorrelation and large surface deformation. Therefore, we used the
137 two Single Look Complex (SLC) radar images, of which pixel spacing is 2.3 m and 14.1 m in
138 the range direction and azimuth direction, respectively, and we calculated the azimuth offset
139 from the correlation between two radar amplitude images by the pixel-tracking method (e.g.,
140 Michel et al., 1999). The window size to measure correlations is 128 x 128 pixels and the
141 sampling spacing is 12 x 12 pixels in size to achieve a spatial resolution of 28 m in the range
142 direction (12 x 2.3 m) and 170 m in the azimuth direction (12 x 14.1 m).

143 The SAR images well exhibited the trace of the rupture on the surface. Figure 2a
144 shows the azimuth offset from the descending images with a maximum of ~8 m relative
145 displacement across the fault, and the ascending image in Figure 2b exhibits the relative
146 displacement of ~5 m. The fault geometry was constrained by the trace on the surface as
147 shown in Figure 2. The strike varies along the fault trace and the rupture can be divided into
148 three segments by a restraining bend near 0.7°S and a releasing bend near 1.2°S. Large
149 offsets appeared between two bends.

150 Although the displacements obtained from the azimuth offsets contain more noise
151 than interferograms, this method allows us to measure large displacements where InSAR
152 does not work; InSAR cannot provide displacements in places where the displacement
153 coherence is low (Wright et al., 2005). In addition, the average uncertainty of pixel offset is
154 1/10 of the pixel size in the azimuth and range directions (Michel et al., 1999).

155

156 2.3 Tsunami Waveform

157 We used the tsunami record of the tide gauge at the port of Pantoloan (the location is
158 shown in Figure 1b) maintained by the Geospatial Information Agency (Badan Informasi
159 Geospasial, BIG) of Indonesia. The sea level is recorded every 60 s. We de-tided the raw data
160 by removing the long period (> 3 hr) tidal constituents, but no resampling or interpolation
161 was applied to the observed data. The Pantoloan station observed an arrival of tsunami wave
162 about 4 min after the earthquake with a maximum wave height (trough to crest) up to 4 m
163 (Figure 3).

164 An obvious waveform change appears about 8 min (after the red-shaded window in
165 Figure 3b) after the earthquake which may result from the combination of waveforms from
166 different sources. Thus, to ensure that only the leading tsunami wave is used, we utilized the
167 record of the first 8 min from the origin time. Although there is only one available station
168 with observed data, the tsunami signal provides important information on the slip offshore
169 area where no SAR observations were available.

170

171 **3 Method**

172 3.1 Teleseismic Source Inversion

173 The location of the rupture initiation was fixed at the hypocenter determined by
174 USGS (119.846°E, 0.256°S, 20 km). A simple fault geometry of an east-dipping plane with a
175 strike of 354° and a dip of 66° (see Aki & Richards, 2002 for angle definitions) was adopted
176 for the teleseismic source inversion. The modeled fault plane is rectangular with a length
177 (along the strike) of 205 km and a width (along the down-dip) of 37 km. The fault plane was
178 divided into subfaults with a size of 5 km x 3.7 km. Variable rupture velocities between 1.5
179 and 4.5 km/s are allowed. To invert for the slip distribution of the Palu earthquake, we
180 computed the Green's functions for the spherically symmetric 1-D velocity model of PREM
181 (Dziewonski & Anderson, 1981) with replacing the shallow layers by the model of
182 CRUST2.0 (Bassin et al., 2000).

183 The slip distribution was estimated by the wavelet-decomposition inversion technique
184 of Ji et al. (2002). The wavelet-decomposition technique gives an optimal resolution of long-
185 and short-period signals in the time domain, which corresponds to slip zones (i.e. asperities)
186 of different scales on the fault plane. Ji et al. (2002) demonstrated that this method provides
187 relatively robust and well-resolved slip features by resolution analyses. Furthermore, the
188 inversion scheme solves inverse problems with a large number of free parameters based on a
189 grid-search scheme with optimization of the Simulated-Annealing algorithm (Rothman,
190 1986). Thus, the wavelet-decomposition scheme permits us to invert for the slip amplitude,
191 slip direction, rise-time, and rupture speed simultaneously and efficiently.

192 3.2 Tsunami Simulation

193 We computed the tsunami propagation by applying the shallow water equations
194 (SWE), which account for tsunami arrival time and waveforms with high accuracy. Explicit
195 finite-difference methods have been implemented to solve the SWE in numerical models.
196 These SWE models perform fast and efficient computations and have been widely used in
197 tsunami research (Satake et al., 2013; Ho et al., 2019). We applied the validated model
198 JAGURS (Baba et al., 2015) to solve linear SWE for the Green's functions in the inversions
199 and nonlinear SWE for the inundation evaluation.

200 To evaluate the dispersion effect, we computed the non-dispersive and dispersive
201 tsunami waveform at Pantoloan and compared them with each other. We first assumed a
202 tsunami source comparable to the 2018 Palu earthquake and simulated the tsunami at
203 Pantoloan by applying the linear SWE to obtain a non-dispersive tsunami waveform. We then
204 converted the non-dispersive waveform into a dispersive waveform utilizing the phase-
205 correction method (Watada et al., 2014; Ho et al., 2017). In Figure S2, the dispersive
206 waveform (red dotted line) is almost identical to the non-dispersive waveform (black line).
207 Because the only tide gauge Pantoloan locates in the source area that recorded the tsunami
208 waves a few minutes after the earthquake, we confirmed that the wave dispersion effect is
209 ignorable in this study.

210 A nested-grid system built in JAGURS was utilized to calculate the waveforms and
211 evaluate the inundation along the shoreline. We utilized three-level nested-layers to acquire
212 accurate calculations where a grid size of 6" (~180 m) for Layer 1 (Figure 1a), 2" (~60 m) for
213 Layer 2 (Figure 1b), and 2/3" (~20 m) for Layer 3 (Figure 1b) were used. The bathymetry for
214 Layer 1 was based on the national bathymetric data of Indonesia (BATNAS) with 6" spatial
215 resolution. For levels 2 and 3, we used the bathymetric and topographic data with a higher
216 resolution of 0.27" obtained from the national digital elevation model of Indonesia

217 (DEMNAS). Both BATNAS and DEMNAS were provided by the BIG of Indonesia. To
 218 improve the inundation modeling, the DEM (digital elevation model) of Layer 2 and 3 were
 219 further corrected by the high-resolution bathymetric contour and topographic data (see
 220 Gusman et al., 2019). We utilized the finest grid, Layer 3, to compute the tsunami Green's
 221 functions for our joint inversion.

222 We introduced a correction term for water depth change due to permanent seafloor
 223 deformation to the Green's functions in our inversion. The Pantoloan station located in the
 224 source area should be subsided by the permanent vertical seafloor deformation as shown in
 225 Gusman et al. (2019). The recorded tsunami waveform contained the sea surface variation
 226 (water wave) and the seafloor deformation. To accurately estimate the tsunami source, we
 227 applied the correction for coseismic displacement to incorporate the permanent seafloor
 228 deformation into the Green's functions.

229 3.3 Contribution of Horizontal Deformation on Tsunami Generation

230 We further calculated the vertical water displacement generated by horizontal
 231 deformation acting on bathymetric slopes. Although strike-slip faulting generates small
 232 vertical displacement, large horizontal deformation can induce additional vertical water
 233 displacement in the presence of bathymetric slopes, strengthening tsunamis. The vertical sea
 234 surface displacement is given by (Tanioka & Satake, 1996):

$$u_h = u_x \frac{\partial H}{\partial x} + u_y \frac{\partial H}{\partial y},$$

235 where u_h is the vertical displacement on the sea surface induced by the horizontal
 236 deformation of the seafloor, H is the water depth and u_x and u_y are the horizontal seafloor
 237 displacements. u_h is positive upward but H is positive downward (depth). The total vertical
 238 displacement at the surface of the seawater is represented by $u_z' = u_h + u_z$, where u_z is the
 239 vertical displacement of the seafloor. u_x , u_y , and u_z are calculated by applying the model of
 240 Okada (1985). Figure S6 shows the vertical displacement due to horizontal deformation u_h
 241 induced by the joint inversion model in section 4.3. Up to 0.6 m of vertical displacements
 242 were generated.

243 3.4 Configuration for Joint Inversion

244 The fault was divided into three segments by a restraining bend near 0.7°S and a
 245 releasing bend near 1.2°S (Figure 2). The strike varies along the fault trace: segment 1 strikes
 246 N2°W (358°) extending 50 km southward from the epicenter to the restraining bend near the
 247 bay, where the surface displacement shows a rupture extending southwestward to the bay
 248 (Figure 2). In segment 2, the strike changed to N8°W (352°) from the offshore area south of
 249 the restraining bend and extended another 50 km to the releasing bend at about 1.2°S where
 250 large surface displacements are presented. Segment 3 extended 20 km from the releasing
 251 bend to approximately 1.4°S with a strike N11°W (349°).

252 We discretized the fault plane into 4 by 29 subfaults, each of which has a size of 5 km
 253 by 5 km with an eastward dip angle of 66°. The rake angle is allowed to vary between -45°
 254 and 45° where the strike-slip with normal or reverse components is incorporated. We
 255 calculated the Green's functions of azimuth offsets and tsunami waveforms under an
 256 assumption of faulting embedded in the elastic half-space theory (Okada, 1985). We then
 257 projected the computed surface displacements to the azimuth direction of the SAR satellite
 258 and resampled the tsunami Green's functions to match the time interval of observed tsunami
 259 waveform.

260 We applied the nonnegative least-square method with Tikhonov regularization to
 261 acquire the slip distribution on the subfaults. In the joint inversion, the equation is given by:

$$262 \begin{bmatrix} \mathbf{B}_S \\ \mathbf{B}_\tau \\ \mathbf{0} \\ \mathbf{0} \end{bmatrix} = \begin{bmatrix} \mathbf{G}_S \\ \mathbf{G}_\tau \\ \lambda \mathbf{I} \\ \gamma \mathbf{L} \end{bmatrix} \mathbf{X}^T,$$

263 where $\mathbf{B}_S = \mathbf{b}^k$ is the column vector of observed SAR images where $k = 1$ to 2 represents
 264 the azimuth offsets of the descending and ascending SAR images, \mathbf{G}_S is the matrix of azimuth
 265 offsets Green's functions \mathbf{S}_j^k , corresponding to the observation \mathbf{b}^k , from the j th subfault,
 266 where $j = 1$ to M , the number of subfaults. $\mathbf{B}_\tau = \beta \mathbf{p}$ is the column vector of the observed
 267 tsunami waveforms \mathbf{p} at Pantoloan weighted by $\beta = 20$. $\mathbf{G}_\tau = \beta \boldsymbol{\eta}_j$ is the matrix of tsunami
 268 Green's functions $\boldsymbol{\eta}_j$ for the j th subfault weighted by β . $\mathbf{X} = [x_j]$ is the unknown row vector
 269 of the amplitude for the j th subfault, where j counts for columns. The regularization factor
 270 $\lambda \mathbf{I} \mathbf{X}^T$ stabilizes the inverse problem, where the $\lambda = 1$ and \mathbf{I} is the identity matrix. We adopted
 271 Laplacian operator $\gamma \mathbf{L} \mathbf{X}^T = 0$ as the spatial smooth constraint, where $\gamma = 1$ is used.

272 4 Results of Two-step Analysis

273 4.1 Teleseismic Source Inversion

274 Figure 4 compares observed and synthetic waveforms of 44 body-waves and 41
 275 surface-waves, respectively, indicating that the synthetic waveforms fit well the observed
 276 body and surface waves. Figure 5 shows the estimated slip distribution, which presents a
 277 single distinct region of slip concentration. This slip distribution suggests that the center of
 278 asperity is located at about 50 km south of the hypocenter. The surface projection of asperity
 279 is right in the bay, which might account for the induced large tsunami height. The maximum
 280 slip in the asperity is about 4.85 m with less slip to the north and below the hypocenter on the
 281 fault plane. The spatial slip distribution and its rupture time suggest that a strike-slip rupture
 282 propagates obliquely from the hypocenter to the south as a unilateral rupture with an average
 283 rupture velocity ~ 3 km/s. Figure S3 shows the moment rate function of the inversion. The
 284 estimated seismic moment is 2.78×10^{20} Nm, which is equivalent to M_w 7.56.

285 The inverted source model was used to compute the tsunami waveform. Figure 6a
 286 shows the computed tsunami waveform compared with the observed tsunami at Pantoloan.
 287 The coseismic vertical deformation is shown in Figure S5. The computed tsunami waveform
 288 is similar to the observed waveform with a slight phase shift and a smaller amplitude. The
 289 fact that the observed tsunami waveforms are explained by the computed one from the slip
 290 distribution estimated from teleseismic waveforms implies that the observed tsunami was
 291 induced directly by the fault slip.

292 The teleseismic inversion model (Figure 5) reconstructs the teleseismic body and
 293 surface waves with a main asperity concentrating near the bay area. However, no asperity
 294 was inverted between 1.0°S to 1.4°S where large offsets were observed by SAR. Contrary to
 295 slip distribution inverted from SAR images that are well constrained in a shallow depth, the
 296 slip distribution obtained from teleseismic waveforms exhibits a general rupture pattern on
 297 the whole fault plane. Because we considered wave propagation in the 1-D velocity model
 298 and used long-period waves (e.g., 1-180 s for body wave and 200-500 s for surface wave) in
 299 our inversion which correspond to wavelengths of hundreds of kilometers, the inversion
 300 result reflects an overall response of the fault plane. Thus, the south asperity might not be
 301 revealed by the teleseismic inversion.

302

303 4.2 SAR-only Inversion

304 We then estimated the fault slip distribution with only SAR data, which consists of
305 two horizontal-direction displacement fields (N20°W and S20°W). The estimated slip
306 distribution in Figure 7a shows the inverted slip distribution, which was decomposed into
307 dip-slip and strike-slip components presented in Figure 8. The inverted source model exhibits
308 a peak slip of up to 9 m at 1.1°S north of the releasing bend and an asperity with about 7 m
309 slip in Palu bay south of the restraining bend. A smaller asperity with about 5 m slip is
310 located south of the epicenter. Large strike-slip was retrieved at a shallow depth of ~10 km.
311 The dip-slip component is generally small. The maximum dip-slip is located at the south of
312 the epicenter with ~3 m normal slip. Very weak oblique slip was found near the releasing
313 bend, where shows a normal slip up 1.6 m. Weak oblique slip with reverse-slip of about -1.7
314 m was retrieved in the restraining bend area. Large normal slip was retrieved at ~1.0°S to
315 explain the surface offsets by SAR images (Figure 2).

316 Figure 6b shows the computed tsunami waveform from the inverted slip model
317 compared with the observation at Pantoloan. The coseismic vertical deformation is shown in
318 Figure S5. The computed tsunami waveform underestimates the observation and fails to
319 match the phase of the first wave. We calculated the characteristic focal mechanism of the
320 fault plane by averaging the moment tensor of all subfaults. The nodal plane strike/dip/rake
321 was 352°/65°/-9°.

322

323 4.3 Joint Inversion

324 To circumvent the poor capability of reconstructing offshore fault slip by SAR images,
325 we performed the joint inversion utilizing the tsunami and SAR data. Because SAR images
326 only provide coseismic surface displacements on land, the derived offshore slip distribution is
327 less constrained than that on land. Tsunami generation is mainly controlled by offshore fault
328 slip; therefore, tsunami data provides good constraint and more information on offshore slip.

329 The joint inversion (Figure 7b) exhibits a slip distribution similar to the one obtained
330 by the SAR-only inversion (Figure 7a), but the slip is noticeably different in the bay area
331 between 0.65°S and 0.9°S. We decomposed the slip into dip-slip and strike-slip components
332 shown in Figure 9. Compared to the weak oblique slip in the restraining bend estimated by
333 the SAR-only inversion, the joint inversion retrieved strike-slip faulting in the bend area.
334 Very weak oblique slip was again retrieved in the releasing bend area at 1.2°S as retrieved by
335 SAR-only inversion. Large dip-slip normal components of 2-4 m appear in the bay area after
336 we added tsunami data to the inversion. This offshore area is less constrained by the SAR
337 images, and the normal components are required to explain the observed tsunami waves.

338 The slip amount along the rupture in Figure 9c exhibits two main asperities with slip
339 larger than 9 m between two bends, one at ~1.1°S north of the releasing bend, which was also
340 retrieved by SAR-only inversion, and another in the southern bay area, which was
341 constrained by tsunami data. A small asperity at the south of the epicenter is also presented to
342 explain the surface offsets. The inversion also well reconstructs the observed azimuth offsets
343 in the descending and ascending SAR images. Figure S4 shows the misfits of the azimuth
344 offsets, where the misfits are smaller than 1 m in most of the source area.

345 The joint inversion model reconstructs well the observed waveform as shown in
346 Figure 6c, which is significantly improved than the SAR-only inversion. The synthetic

347 tsunami matches well the phase and amplitude of the leading part in the observation. The
348 unusual waveform appeared from 8 to 15 minutes after the earthquake with a 3-m wave
349 (Figure 6c) could be a result of the reflection or nonlinear effects of the bay. The simulated
350 tsunami is much smaller than that observed at Mamuju (Figure S7), where the tsunami may
351 come from another source. Other than the earthquake, a landslide was also considered as a
352 secondary or main source (Carvajal et al. 2019; Gusman et al., 2019; Sassa & Takagawa,
353 2019). The coseismic vertical deformation is shown in Figure S5.

354 The nodal plane strike/dip/rake calculated from the joint inversion slip distribution
355 was $352^{\circ}/64^{\circ}/-13^{\circ}$, which is very close to the one by SAR-only inversion and compatible
356 with the plane by the Global CMT solution of $348^{\circ}/57^{\circ}/-15^{\circ}$ (Dziewonski et al., 1981;
357 Ekström et al., 2012) and the USGS W-phase Moment Tensor solution of $350^{\circ}/67^{\circ}/-17^{\circ}$ by
358 the United States Geological Survey (2018). Although the characteristic focal mechanism
359 shows strike-slip faulting on the fault plane, the local dip-slip components are still able to
360 generate a regional devastating tsunami in Palu bay. The finite-fault parameters of the joint
361 inversion model are provided in Supporting Information.

362

363 4.4 Tsunami Inundation

364 To evaluate the tsunami inundation, we applied the nonlinear SWE to the finest grids
365 Layer 3, which covered the entire coast of Palu bay, as noted in section 3.2. We adopted the
366 slip model inverted by the joint inversion (Figure 7b) as the initial condition. According to
367 the tide prediction of BIG, the tsunami occurred during the high tide, so we considered the
368 sea-level rise for 1 m when computing the flow depth. We divided the coast of Palu bay into
369 three parts by the west, south, and east coasts. The Palu city is located on the south coast. The
370 overall impacts to the coastal communities along the west and east coasts were less severe
371 than the south coast because of the steep topography in those areas on the west and east
372 coasts.

373 Figure 10a, 11a, and 12a show the estimated flow depth for the south coast (Layer
374 3-4), west coast (Layer 3-5 to 3-7), and east coast (Layer 3-1 to 3-3), respectively. The
375 estimated flow depth was also compared to the field measurements (Mikami et al., 2019;
376 Paulik et al., 2019) in Figure 10b, 11b, and 12b. We also computed the maximum flow depth
377 on the coastline represented by blue blocks in Figure 10b, 11b, and 12b.

378 On the south coast, high flow depths were measured near the mouth of Palu River and
379 decreased westward and eastward. Up to 4-m-high flow depths were measured at the two
380 sides of the mouth of Palu River, where we partially reproduced the flow depth by about 1-2
381 m height at the measuring positions. The measured flow depths reduce to smaller than 2 m on
382 the area further east of the river mouth. We had a good estimation near 119.865°E with ~ 1 m
383 flow depth. On the west side of the river mouth, we reproduced the flow depths on the coast
384 between 119.84°E and 119.85°E . Further west of 119.84°E , the flow depth increased to up to
385 5 m, but the estimated flow depth decreased to only 0-2 m high.

386 Figure 11 shows the result for the west coast. Our model caused up to 5 m flow depth
387 on the coastline, but the inundation distance was so short and we could not reproduce the
388 flow depth at the measured locations. On the east coast shown in Figure 12, we estimated
389 flow depths of higher than 5 m on the coastline between 0.75°S and 0.85°S . Our model
390 induced higher flow depth and longer inundation distance on the east coast than the west
391 coast.

392 The estimated inundation shows a general pattern similar to the observation that the
393 inundation is stronger on the south coast and weaker on the east and west coasts. Our model
394 reproduces the flow depths in some places on the south coast but underestimates the
395 inundations on the west and east coasts and some parts of the south coast. This result suggests
396 that the general pattern of the tsunami source is reproduced and implies a secondary source to
397 account for the local high flow depths, such as a landslide.

398

399 **5 Discussion**

400 In the teleseismic source inversion, a simple rectangular fault geometry is applicable.
401 Koketsu et al. (2011) and Yokota et al. (2011) have performed separate and joint inversions
402 utilizing teleseismic, strong motion, geodetic, and/or tsunami data to estimate the source of
403 the 2011 Tohoku earthquake. They exhibited checkerboard resolution tests and real case
404 inversions and pointed out that teleseismic-data-only inversions show limited spatial
405 resolution. Our teleseismic source inversion utilizes low-frequency body and surface waves.
406 The result resolves a characteristic source mechanism with a general slip distribution rather
407 than the details such as small asperities. Thus, a simple rectangular fault geometry is
408 applicable for the teleseismic source inversion. In other words, because teleseismic-data-only
409 inversion is not sensitive to subtle slip variations but resolves a smooth slip model, we can
410 expect a similar inverted slip model if we apply a complex geometry with the same method.
411 However, the induced tsunami by the slip model is controlled by local offshore slip, so a
412 similar slip distribution could induce very different tsunami waves. The source model
413 estimated by the teleseismic source inversion located the major asperity at shallow depth in
414 the bay area and the computed tsunami implied that the observed tsunami waveform can be
415 explained by fault rupture. We then carried out the joint inversion of SAR and tsunami data
416 to estimate the detailed slip distribution.

417 To estimate a detailed slip distribution, we applied a complex fault geometry for the
418 joint inversion and the SAR-only inversion. The offsets in different directions recorded by
419 SAR images revealed a clear rupture trace that allowed us to determine a complex fault
420 geometry, which was appropriate for the SAR-only inversion and joint inversion to retrieve a
421 detailed slip distribution. Due to the clear boundary of offsets of different directions, if we
422 apply a simple geometry to the SAR-only or joint inversion, we will fail to fit the offsets
423 somewhere, e.g., the bend areas. The SAR images have no contribution to the bay (sea) area,
424 where the offshore slip is only constrained by the adjacent land offset records in SAR-only
425 inversion. In contrast, tsunami waves, which are induced by offshore displacement, provide
426 good constraints for the offshore area. By adding tsunami data to the inversion, we can
427 retrieve the slip distribution that generates the observed tsunami waveform. Although the
428 SAR images dominated the joint inversion because they recorded the land offsets of most of
429 the rupture area, the tsunami data still provide an important contribution to the offshore slip.
430 Figure 7 exhibits noticeable slip differences in the bay area that indicates the indispensable
431 contribution of tsunami data to the joint inversion.

432 Our inversion results are comparable to other studies in some parts. Our SAR-only
433 inverted model exhibits weak oblique slip near the restraining and releasing bends, which is
434 comparable to the results of Socquet et al. (2019) and He et al. (2019). Socquet et al. (2019)
435 estimated oblique slip with comparable strike-slip and dip-slip components in the bay area
436 and the releasing bend at 1.2°S and 0.2°S . He et al. (2019) had a similar source model on
437 their onshore segments. The restraining bend area is located in the bay area, where different
438 slip was retrieved. Our joint inversion model retrieved normal slip near the bay, which were

439 also estimated by Ulrich et al. (2019), who addressed a regional releasing beneath the bay and
440 retrieved 2-m normal slip in the bay area, and Fang et al. (2019) also estimated normal slip up
441 to 2 m in Palu bay. Lee et al. (2019) estimated an oblique-to-normal slip from the epicenter to
442 the bay at a ~15 km depth.

443 An offshore normal fault based on the bathymetry was added by Song et al. (2019)
444 and He et al. (2019). According to Song et al. (2019), the additional normal fault improved
445 the misfit of InSAR data for the northwest island further north of 0.3°S. The inverted slip
446 distribution is identical to the one without an additional segment in the area further south of
447 0.5°S. Although they claimed that the normal fault may be the source of the tsunami, the
448 northwest offshore segment is too far to be the source for the leading tsunami wave. However,
449 the predicted tsunami at Mamuju may be improved by an offshore segment.

450 The observed tsunami wave was neither explained by the strike-slip displacement
451 (Lee et al., 2019), the oblique slip (Socquet et al., 2019), nor an additional offshore normal-
452 faulting segment (Song et al. 2019). Ulrich et al. (2019) retrieved normal slip in the bay area
453 and their model reproduced the magnitude of the tsunami wave. Our joint inversion source
454 model reconstructed the tsunami waveform at Pantoloan and the flow depths in some areas on
455 the south coast, but failed to reproduce the local high flow depth in other places. The
456 underestimation can be contributed by some factors, for example, the precision of measuring
457 positions, accuracy of topographic data, the inverted model, and additional sources. The error
458 of measuring position can result from device error and inherent positioning error of different
459 signal conditions, but it can only explain some specific positions.

460 The accuracy and precision of the topographic data can be discussed separately. The
461 topographic data, which was provided by BIG, should be accurate for tsunami inundation
462 computation, but the DEM does not include the urban land cover, e.g., buildings and streets,
463 which could generate estimation errors. According to the study of Ali et al. (2015), DEMs in
464 different resolutions did not show significant differences in flood assessment. The quality and
465 accuracy of a DEM are more important than the resolution and precision. Savage et al. (2016)
466 demonstrated that the performance of deterministic simulations degrades as resolution coarser
467 than 50 m, and has little improvement when resolution finer than 50 m. We applied the high-
468 resolution bathymetric contour and topographic data from BIG to construct our Layer 2 and
469 Layer 3, where the Layer 3 has the finest resolution of 20 m (east-west direction) by 13 m
470 (north-south direction). Although the buildings and streets are not included on top of the
471 topography in the DEM, the resolution should be applicable to approximately estimate the
472 inundation for source assessment. Future work to explore the detailed flood in the city should
473 consider the urban land cover.

474 Since we reconstructed well the tsunami wave at Pantoloan and partially reproduced
475 the flow depth of the south coast, the characteristic pattern of the tsunami should be retrieved
476 by our source model. A secondary source is a reasonable explanation for the local high flow
477 depths. Although landslide events were suggested by previous studies (Carvajal et al., 2019;
478 Gusman et al., 2019; Sassa & Takagawa, 2019), the precise location and dimension are still
479 controversial. Future investigation and exploration will provide more evidence and uncover
480 the puzzle.

481 **6 Conclusions**

482 To examine if the tsunami can be induced by the rupture displacements, we performed
483 a two-step analysis of the 2018 Palu earthquake by performing two inversion methods with
484 two different data sets: step one, the teleseismic source inversion, and step two, the SAR-only
485 inversion and the joint inversion of SAR and tsunami data.

486 Our teleseismic source inversion indicated that a strike-slip rupture propagated from
487 the hypocenter to the south, with the major asperity located at about 50 km south of the
488 hypocenter in the shallow part. The observed tsunami waveform at Pantoloan was explained
489 by the slip distribution, suggesting that the strike-slip faulting with localized dip-slip was the
490 major cause of the tsunami. We then estimated the fault slip distribution with only SAR data,
491 but the computed tsunami could not reproduce the observed tsunami waveform, because the
492 offshore slip was not well resolved. The joint inversion of SAR and tsunami data shows a
493 strike-slip fault which consists of three segments extending from the epicenter to the south of
494 1.4°S with two bends and two asperities around Palu city. The tsunami data provides
495 necessary information to reconstruct the slip distribution inside the bay that reproduces well
496 the observed tsunami waveform at Pantoloan and part of inundations in Palu city. However,
497 to fully explain the high inundations near Palu bay, additional sources, such as landslides, are
498 also suggested. We provide the parameters for the finite faults of the joint inversion in the
499 supporting information Dataset S1.

500 Finally, this study points out that local devastating tsunamis can result from a strike-
501 slip fault. This suggests that offshore and/or onshore strike-slip faults should be considered in
502 tsunami hazard assessment to account for regional tsunamis.

503

504 **Acknowledgement**

505 The Copernicus Sentinel data (Sentinel-1) are provided from the European Space
506 Agency (ESA). The tide gauge data at Pantoloan station are from the Geospatial Information
507 Agency of Indonesia (Badan Informasi Geospasial, BIG) <http://tides.big.go.id/>. The
508 DEMNAS and BATNAS topographic and bathymetric datasets are downloaded from the
509 Geospatial Information Agency of Indonesia (BIG) <http://tides.big.go.id/>. Earthquake Catalog
510 courtesy of the U.S. Geological Survey. The authors appreciate the valuable suggestions from
511 Drs. Yuichiro Tanioka and Nobuhito Mori. This work was supported by JST J-RAPID
512 JPMJ1805, by KAKENHI (16H01838 19K04034), and by Core-to-Core Collaborative
513 research program of the Earthquake Research Institute, The University of Tokyo and the
514 Disaster Prevention Research Institute, Kyoto University. The authors appreciate the valuable
515 comments and suggestions from the two anonymous reviewers.

516

517 **Reference**

- 518 Aki, K., & Richards, P. G. (2002). *Quantitative seismology, 2nd Ed.* University Science
519 Books.
- 520 Ali, A. M., Solomatine, D. P., & Di Baldassarre, G. (2015). Assessing the impact of different
521 sources of topographic data on 1-D hydraulic modelling of floods. *Hydrology and*
522 *Earth System Sciences*, 19(1), 631-643.
- 523 Baba, T., Takahashi, N., Kaneda, Y., Ando, K., Matsuoka, D., & Kato, T. (2015). Parallel
524 implementation of dispersive tsunami wave modeling with a nesting algorithm for the
525 2011 Tohoku tsunami. *Pure and Applied Geophysics*, 172(12), 3455-3472.
526 <http://doi.org/10.1007/s00024-015-1049-2>
- 527 Bao, H., Ampuero, J. P., Meng, L., Fielding, E. J., Liang, C., Milliner, C. W., ... & Huang, H.
528 (2019). Early and persistent supershear rupture of the 2018 magnitude 7.5 Palu
529 earthquake. *Nature Geoscience* DOI, 10. <https://doi.org/10.1038/s41561-018-0297-z>

- 530 Bassin, C., G. Laske, and G. Masters (2000). The current limits of resolution for surface wave
531 tomography in North America. *Eos, Transactions of the American Geophysical*
532 *Union*, 81, F897 (<http://igppweb.ucsd.edu/~gabi/crust2.html>).
- 533 Carvajal, M., Araya-Cornejo, C., Sepúlveda, I., Melnick, D., & Haase, J. S. (2019). Nearly
534 instantaneous tsunamis following the Mw 7.5 2018 Palu earthquake. *Geophysical*
535 *Research Letters*, 46. <https://doi.org/10.1029/2019GL082578>
- 536 Dziewonski, A. M. and D. L. Anderson (1981). Preliminary reference Earth model. *Phys.*
537 *Earth Planet. Inter.* 25(4), 297–356.
- 538 Dziewonski, A. M., Chou, T. A., & Woodhouse, J. H. (1981). Determination of earthquake
539 source parameters from waveform data for studies of global and regional seismicity.
540 *Journal of Geophysical Research: Solid Earth*, 86(B4), 2825-2852.
541 <https://doi.org/10.1029/JB086iB04p02825>
- 542 Ekström, G., Nettles, M., & Dziewoński, A. M. (2012). The global CMT project 2004–2010:
543 Centroid-moment tensors for 13,017 earthquakes. *Physics of the Earth and Planetary*
544 *Interiors*, 200, 1-9. <https://doi.org/10.1016/j.pepi.2012.04.002>
- 545 Fang, J., Xu, C., Wen, Y., Wang, S., Xu, G., Zhao, Y., & Yi, L. (2019). The 2018 Mw 7.5
546 Palu Earthquake: A Supershear Rupture Event Constrained by InSAR and Broadband
547 Regional Seismograms. *Remote Sensing*, 11(11), 1330.
- 548 Gusman, A. R., Supendi, P., Nugraha, A. D., Power, W., Latief, H., Sunendar, H., ... &
549 Wang, X. (2019). Source model for the tsunami inside Palu Bay following the 2018
550 Palu earthquake, Indonesia. *Geophysical Research Letters*, 46(15), 8721-8730.
551 <http://dx.doi.org/10.1029/2019GL082717>
- 552 He, L., Feng, G., Li, Z., Feng, Z., Gao, H., & Wu, X. (2019). Source parameters and slip
553 distribution of the 2018 Mw 7.5 Palu, Indonesia earthquake estimated from space-
554 based geodesy. *Tectonophysics*, 772, 228216.
555 <https://doi.org/10.1016/j.tecto.2019.228216>
- 556 Heidarzadeh, M., Muhari, A., & Wijanarto, A. B. (2019). Insights on the source of the 28
557 September 2018 Sulawesi tsunami, Indonesia based on spectral analyses and
558 numerical simulations. *Pure and Applied Geophysics*, 176(1), 25-43.
559 <https://doi.org/10.1007/s00024-018-2065-9>
- 560 Ho, T. C., Satake, K., & Watada, S. (2017). Improved phase corrections for transoceanic
561 tsunami data in spatial and temporal source estimation: Application to the 2011
562 tohoku earthquake. *Journal of Geophysical Research: Solid Earth*, 122(12), 10-155.
563 <https://doi.org/10.1002/2017JB015070>
- 564 Ho, T. C., Satake, K., Watada, S., & Fujii, Y. (2019). Source estimate for the 1960 Chile
565 earthquake from joint inversion of geodetic and transoceanic tsunami data. *Journal of*
566 *Geophysical Research: Solid Earth*, 124(3), 2812-2828.
567 <https://doi.org/10.1029/2018JB016996>
- 568 Ji, C., Wald, D. J., & Helmberger, D. V. (2002). Source description of the 1999 Hector Mine,
569 California, earthquake, part I: Wavelet domain inversion theory and resolution
570 analysis. *Bulletin of the Seismological Society of America*, 92(4), 1192-1207.
- 571 Koketsu, K., Yokota, Y., Nishimura, N., Yagi, Y., Miyazaki, S. I., Satake, K., ... & Okada, T.
572 (2011). A unified source model for the 2011 Tohoku earthquake. *Earth and Planetary*
573 *Science Letters*, 310(3-4), 480-487. <https://doi.org/10.1016/j.epsl.2011.09.009>

- 574 Lee, S. J., Wong, T. P., Lin, T. C., & Liu, T. Y. (2019). Complex Triggering Supershear
575 Rupture of the 2018 M w 7.5 Palu, Indonesia, Earthquake Determined from
576 Teleseismic Source Inversion. *Seismological Research Letters*.
- 577 Michel, R., Avouac, J. P., and Taboury, J. (1999) Measuring ground displacements from SAR
578 amplitude images: application to the Landers earthquake. *Geophysical Research*
579 *Letters*, 26, 875-878. <http://doi.org/10.1029/1999GL900138>.
- 580 Mikami, T., Shibayama, T., Esteban, M., Takabatake, T., Nakamura, R., Nishida, Y., ... &
581 Krautwald, C. (2019). Field survey of the 2018 Sulawesi tsunami: inundation and run-
582 up heights and damage to coastal communities. *Pure and Applied Geophysics*, 176(8),
583 3291-3304. <https://doi.org/10.1007/s00024-019-02258-5>
- 584 Muhari, A., Imamura, F., Arikawa, T., Hakim, A. R., & Afriyanto, B. (2018). Solving the
585 puzzle of the September 2018 pale, Indonesia, tsunami mystery: Clues from the
586 tsunami waveform and the initial field survey data. *Journal of Disaster Research*, 13,
587 sc20181108. <https://doi.org/10.20965/jdr.2018.sc20181108>
- 588 Okada, Y. (1985). Surface deformation due to shear and tensile faults in a half-space. *Bulletin*
589 *of the seismological society of America*, 75(4), 1135-1154.
- 590 Omira, R., Dogan, G. G., Hidayat, R., Husrin, S., Prasetya, G., Annunziato, A., ... & Zaytsev,
591 A. (2019). The September 28th, 2018, Tsunami In Palu-Sulawesi, Indonesia: A Post-
592 Event Field Survey. *Pure and Applied Geophysics*, 176(4), 1379-1395.
593 <https://doi.org/10.1007/s00024-019-02145-z>
- 594 Paulik, R., Gusman, A., Williams, J. H., Pratama, G. M., Lin, S. L., Prawirabhakti, A., ... &
595 Suwarni, N. W. I. Tsunami Hazard and Built Environment Damage Observations
596 from Palu City after the September 28 2018 Sulawesi Earthquake and Tsunami. *Pure*
597 *and Applied Geophysics*, 1-17.
- 598 Prasetya, G. S., De Lange, W. P., & Healy, T. R. (2001). The makassar strait tsunamigenic
599 region, Indonesia. *Natural Hazards*, 24(3), 295-307.
- 600 Rothman, D. H. (1986). Automatic estimation of large residual statics corrections.
601 *Geophysics*, 51(2), 332-346.
- 602 Sassa, S., & Takagawa, T. (2019). Liquefied gravity flow-induced tsunami: First evidence
603 and comparison from the 2018 Indonesia Sulawesi earthquake and tsunami disasters.
604 *Landslides*, 16(1), 195–200. <https://doi.org/10.1007/s10346-018-1114-x>
- 605 Satake, K., Fujii, Y., Harada, T., & Namegaya, Y. (2013). Time and space distribution of
606 coseismic slip of the 2011 Tohoku earthquake as inferred from tsunami waveform
607 data. *Bulletin of the seismological society of America*, 103(2B), 1473-1492.
- 608 Savage, J. T. S., Bates, P., Freer, J., Neal, J., & Aronica, G. (2016). When does spatial
609 resolution become spurious in probabilistic flood inundation predictions?.
610 *Hydrological Processes*, 30(13), 2014-2032.
- 611 Socquet, A., Simons, W., Vigny, C., McCaffrey, R., Subarya, C., Sarsito, D., ... & Spakman,
612 W. (2006). Microblock rotations and fault coupling in SE Asia triple junction
613 (Sulawesi, Indonesia) from GPS and earthquake slip vector data. *Journal of*
614 *Geophysical Research: Solid Earth*, 111(B8).
- 615 Socquet, A., Hollingsworth, J., Pathier, E., & Bouchon, M. (2019). Evidence of supershear
616 during the 2018 magnitude 7.5 Palu earthquake from space geodesy. *Nature*
617 *Geoscience*, 12(3), 192. <https://doi.org/10.1038/s41561-018-0296-0>

- 618 Song, X., Zhang, Y., Shan, X., Liu, Y., Gong, W., & Qu, C. (2019). Geodetic observations of
 619 the 2018 Mw 7.5 Sulawesi earthquake and its implications for the kinematics of the
 620 Palu fault. *Geophysical Research Letters*, 46(8), 4212-4220.
- 621 Tanioka, Y., & Satake, K. (1996). Tsunami generation by horizontal displacement of ocean
 622 bottom. *Geophysical Research Letters*, 23(8), 861-864.
- 623 Ulrich, T., Vater, S., Madden, E. H., Behrens, J., van Dinther, Y., Van Zelst, I., ... & Gabriel,
 624 A. A. (2019). Coupled, physics-based modeling reveals earthquake displacements are
 625 critical to the 2018 Palu, Sulawesi Tsunami. *Pure and Applied Geophysics*, 176(10),
 626 4069-4109.
- 627 United States Geological Survey (2018). M7.5—70 km No of Palu Indonesia,
 628 <https://earthquake.usgs.gov/earthquakes/eventpage/us1000h3p4/executive>
- 629 Watada, S., Kusumoto, S., & Satake, K. (2014). Traveltime delay and initial phase reversal of
 630 distant tsunamis coupled with the self-gravitating elastic Earth. *Journal of*
 631 *Geophysical Research: Solid Earth*, 119(5), 4287-4310.
 632 <https://doi.org/10.1002/2013JB010841>
- 633 Wright, P., Macklin, T., Willis, C., & Rye, T. (2005). Coherent change detection with SAR.
 634 In *European Radar Conference, 2005. EURAD 2005.* (pp. 17-20). IEEE.
- 635 Yokota, Y., Koketsu, K., Fujii, Y., Satake, K., Sakai, S. I., Shinohara, M., & Kanazawa, T.
 636 (2011). Joint inversion of strong motion, teleseismic, geodetic, and tsunami datasets
 637 for the rupture process of the 2011 Tohoku earthquake. *Geophysical Research Letters*,
 638 38(7). <https://doi.org/10.1029/2011GL050098>
- 639 Yolsal-Çevikbilen, S., & Taymaz, T. (2019). Source Characteristics of the 28 September
 640 2018 Mw 7.5 Palu-Sulawesi, Indonesia (SE Asia) Earthquake Based on Inversion of
 641 Teleseismic Bodywaves. *Pure and Applied Geophysics*, 1-16.
- 642 Yalciner A. C. et al. (2018). The 28th September 2018 Palu Earthquake and Tsunami ITST,
 643 07-11 November 2018 Post Tsunami Field Survey Report (Short).

644
 645

646 **Figure 1.** The three layers for computing the tsunami waveforms and inundations. (a) The
 647 entire computational domain of Layer 1 and the region of Layer 2. The Red star indicates the
 648 epicenter, and the white circles show the aftershocks of M4.0 to M5.9 within two months
 649 after the mainshock provided by the USGS Earthquake Catalog. (b) The domain of Layer 2
 650 and the seven black rectangles indicate the areas of Layer 3 where the numbers from 1 to 7 at
 651 the southeast corner represent the Layer 3-1 to 3-7. The blue inverted triangle indicates the
 652 tide gauge at Pantoloan. The magenta dots show the locations of inundation/flow depth
 653 observations.

654

655 **Figure 2.** Azimuth offsets from (a) descending (S20°W) and (b) ascending (N20°W) images
 656 observed by Sentinel-1. The red stars show the epicenter of the earthquake. The black and
 657 green arrows indicate the azimuth and range directions, respectively.

658

659 **Figure 3.** The tsunami waveform recorded by the Pantoloan tide gauge. (a) shows the raw
660 data, (b) is the de-tided waveform. The red-shaded window shows the signals used in the
661 inversions.

662

663 **Figure 4.** Waveform comparisons between observed (black) and synthetic (red) (a)
664 teleseismic body waves and (b) teleseismic surface waves. In each panel, station and phase
665 IDs are labeled on the left. Phase IDs are abbreviated as follows: ‘P’ for P wave, ‘SH’ for SH
666 wave, ‘RA’ for Rayleigh wave, and ‘LO’ for Love wave, respectively. The numbers above
667 and below the beginning of each trace indicate azimuth relative to the source and epicentral
668 distance, both in degrees. The observed peak ground displacement in micrometers is shown at
669 the end of each trace.

670

671 **Figure 5.** The slip distribution of the Palu earthquake in (a) map view and (b) cross-section.
672 The gray star denotes the hypocenter. In (a) and (b), the background color on the fault plane
673 indicates the amount of slip. In (b), the rake angle is indicated by the arrow at each subfault
674 center. The contours represent the elapsed time the rupture from its onset in seconds with a
675 contour interval of 5 s.

676

677 **Figure 6.** Waveform comparisons between the observed and calculated waveforms by (a) the
678 teleseismic inversion, (b) the SAR-only inversion, and (c) the joint inversion model. The
679 blue-shaded windows indicate the data used in our inversion.

680

681 **Figure 7.** Slip distributions derived from (a) the source inversions with only SAR images and
682 (b) the joint inversion with SAR and tsunami data. Color and arrows indicate the slip
683 amplitude and the rake angle, respectively. The star denotes the epicenter.

684

685 **Figure 8.** Slip distribution of (a) dip-slip and (b) strike-slip components, and (c) slip amount
686 estimated by SAR-only inversion. Negative indicates the reverse-faulting component in (a).
687 S-Bend represents the releasing bend and N-bend indicates the restraining bend. The star
688 indicates the hypocenter.

689

690 **Figure 9.** Slip distribution of (a) dip-slip and (b) strike-slip components, and (c) slip amount
691 estimated by joint inversion.

692

693 **Figure 10.** The estimated flow depth on the south coast of Palu bay in Layer 3-4. (a) The
694 computed flow depth is shown in color. Dark crosses indicate the measuring positions of field
695 surveys. (b) The observed (dark crosses) and computed (red circles) flow depth at measuring
696 positions of field surveys. The blue blocks represent the computed maximum flow depths on
697 the coastline.

698

699 **Figure 11.** The estimated flow depth on the west coast of Palu bay for Layer 3-5 to 3-7. (a)
700 Dark crosses indicate the measuring positions of field surveys. (b) The dark crosses show the

701 observed flow depth at measuring positions of field surveys. The blue blocks represent the
702 computed maximum flow depths on the coastline.

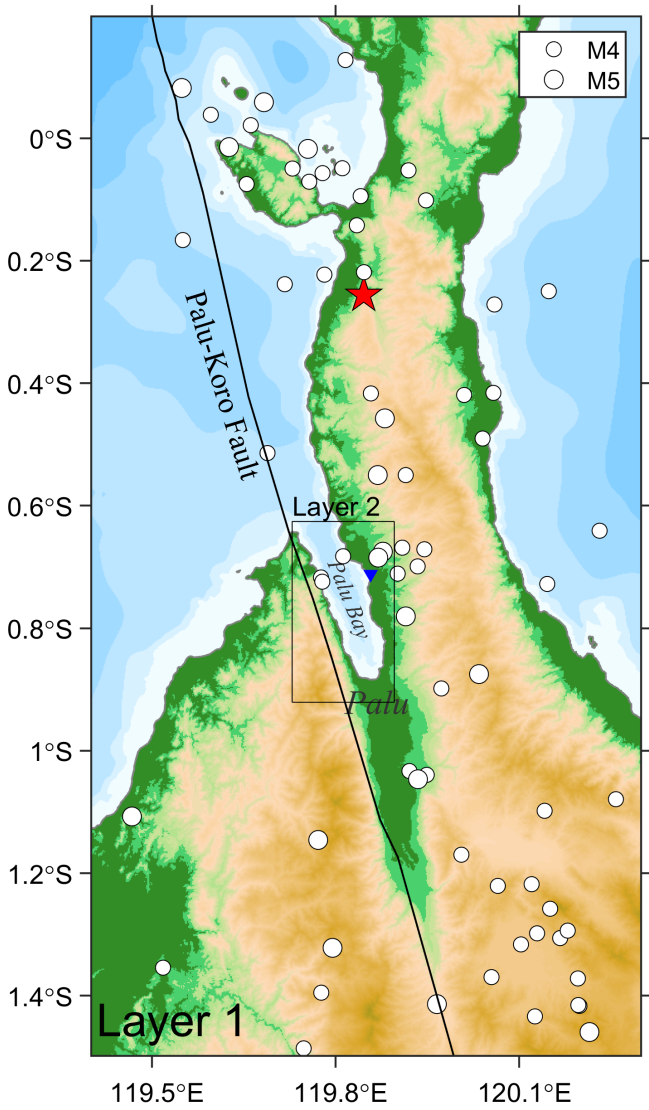
703

704 **Figure 12.** The estimated flow depth on the east coast of Palu bay for Layer 3-1 to 3-3. (a)
705 Dark crosses indicate the measuring positions of field surveys. (b) The dark crosses show the
706 observed flow depth at measuring positions of field surveys. The blue blocks represent the
707 computed maximum flow depths on the coastline.

708

Figure 1.

(a)



(b)

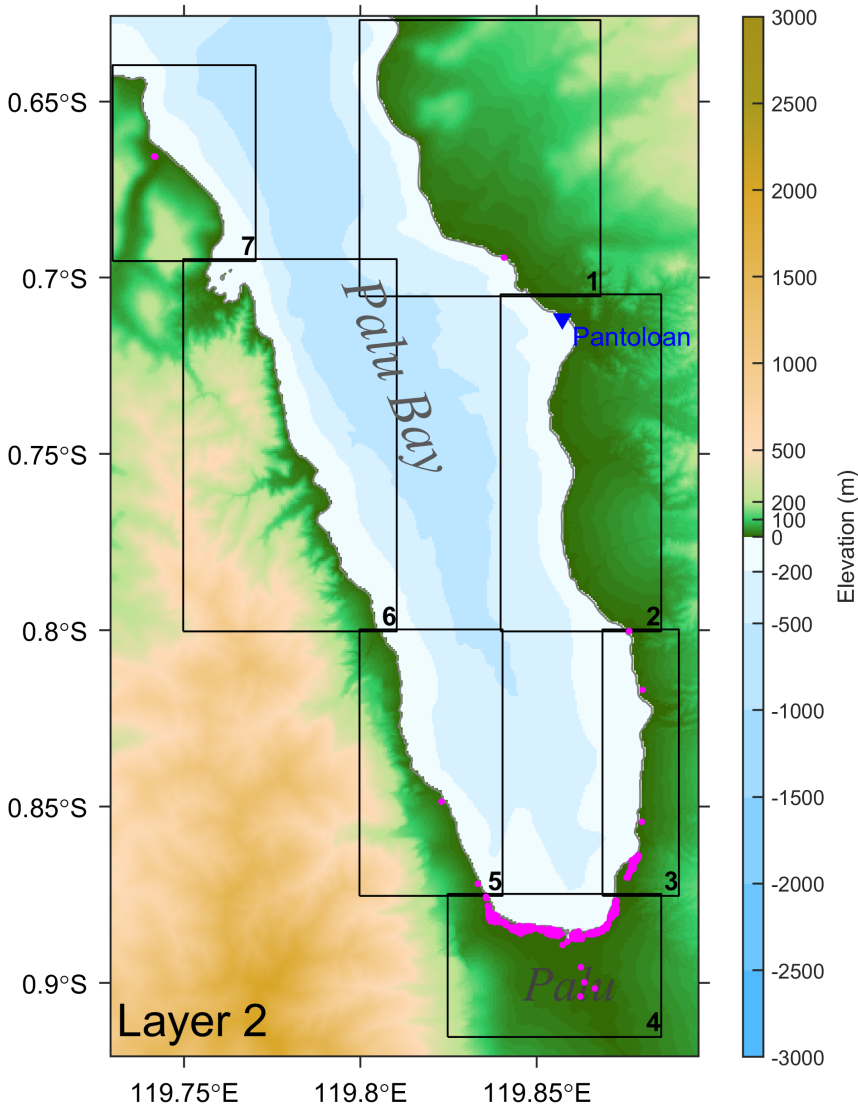
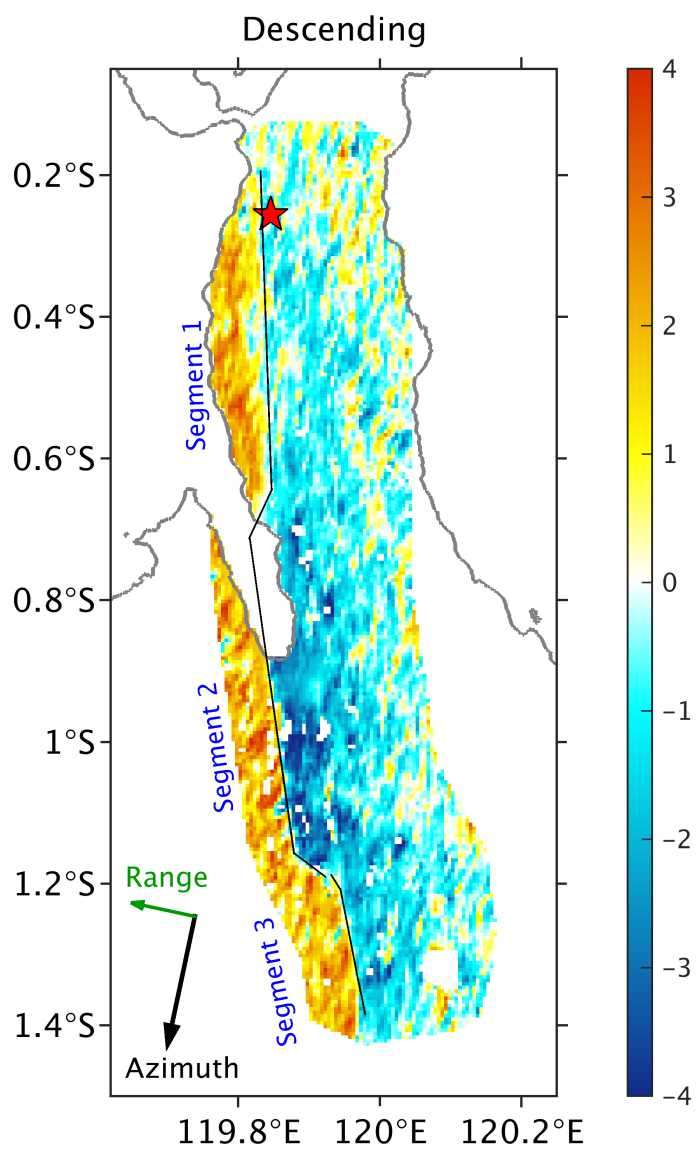


Figure 2.

(a)



(b)

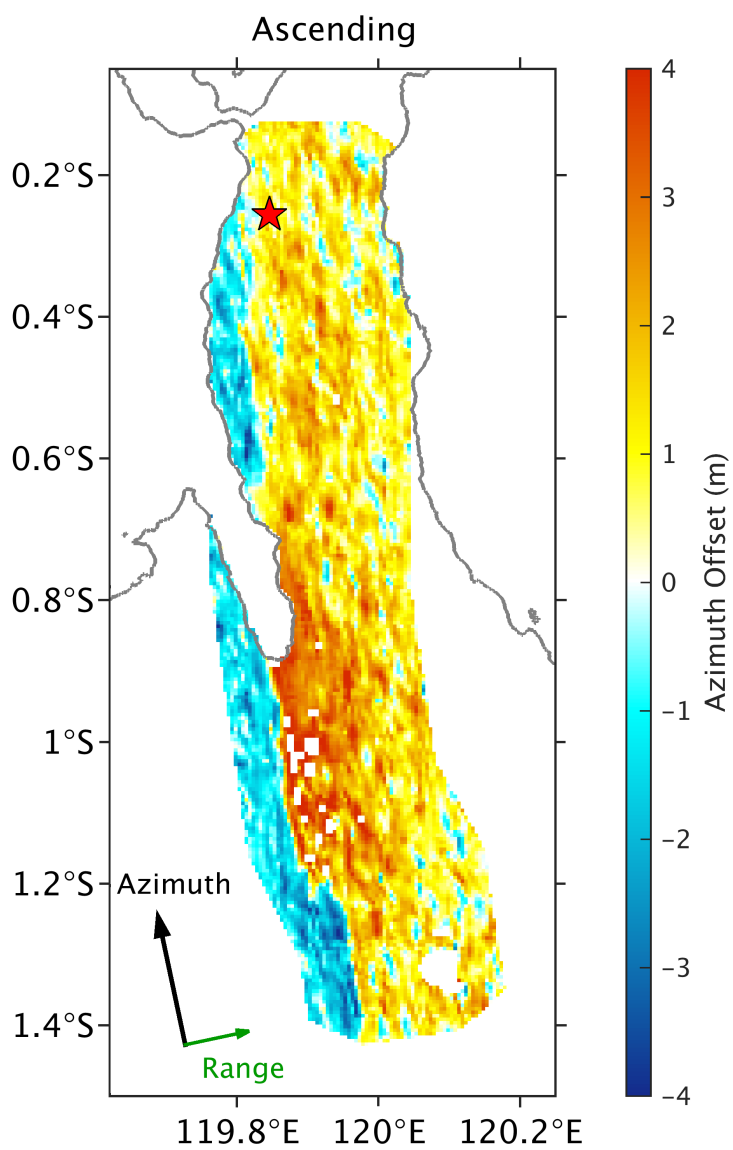
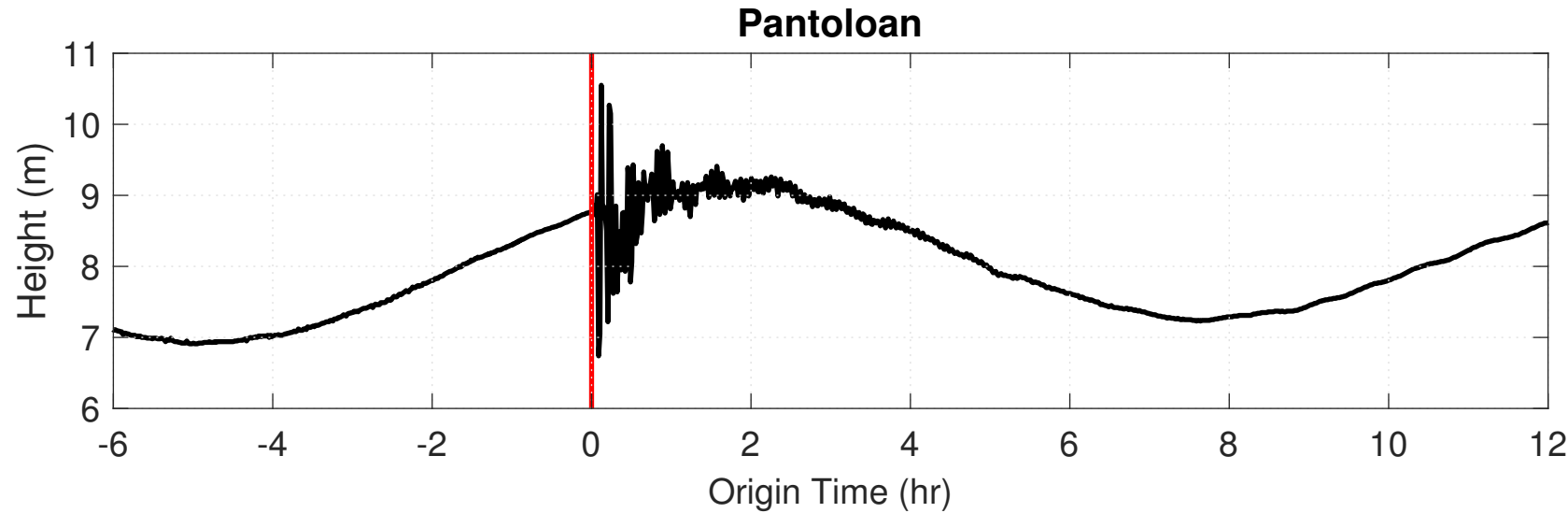


Figure 3.

(a)



(b)

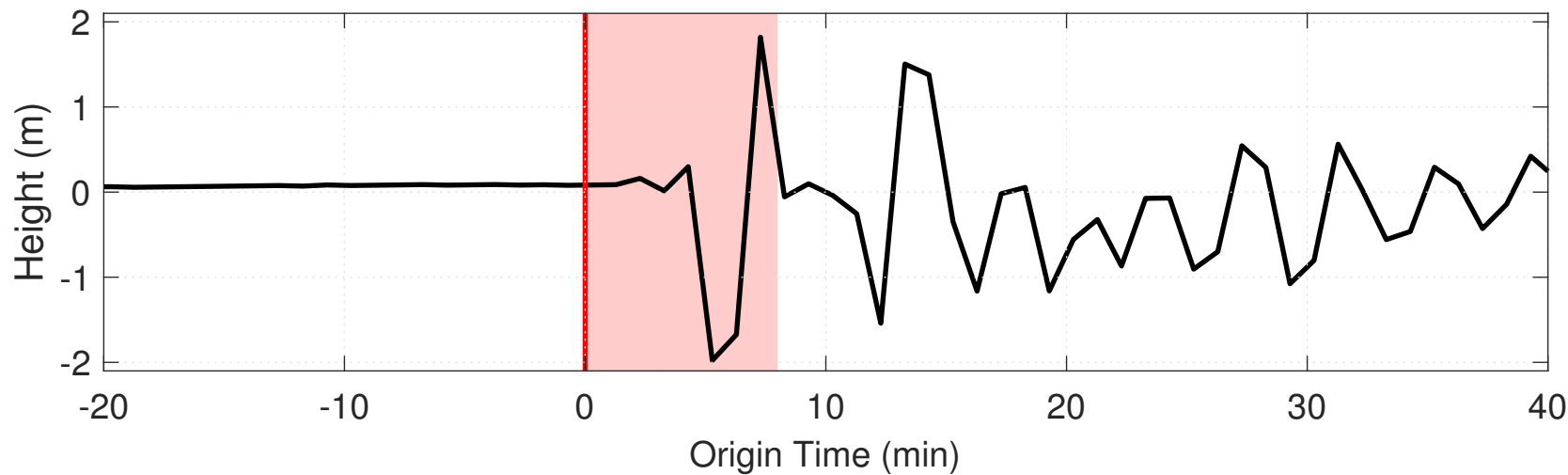


Figure 4.

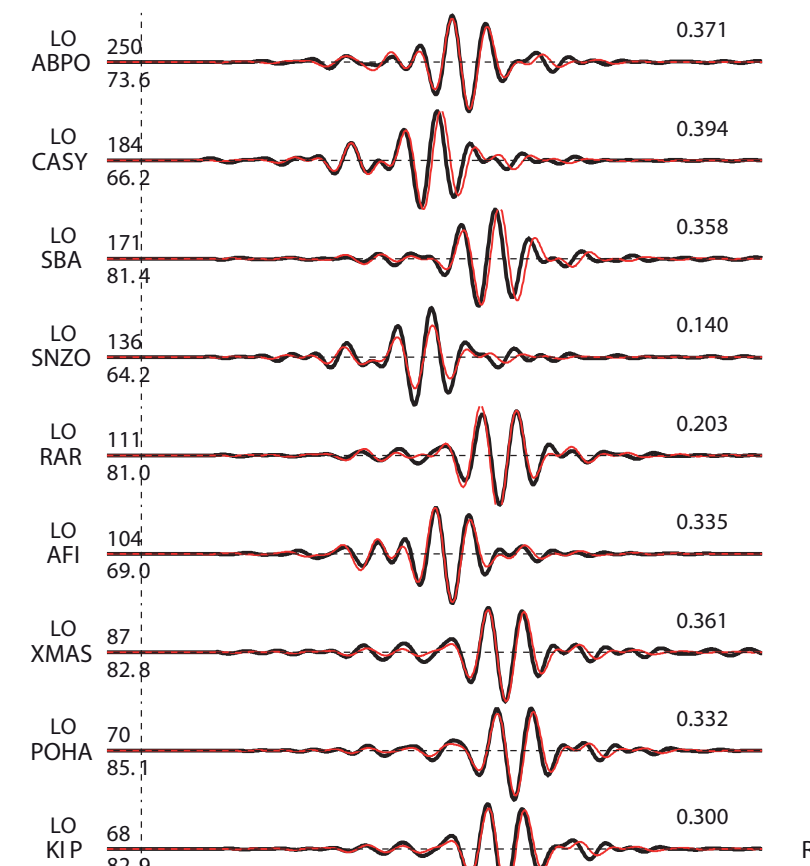
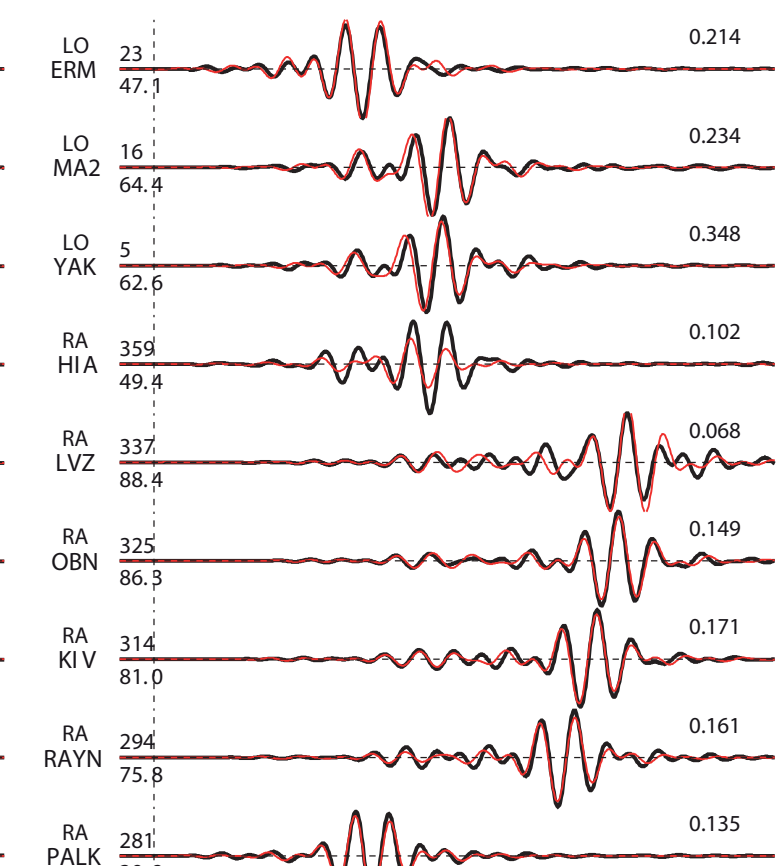
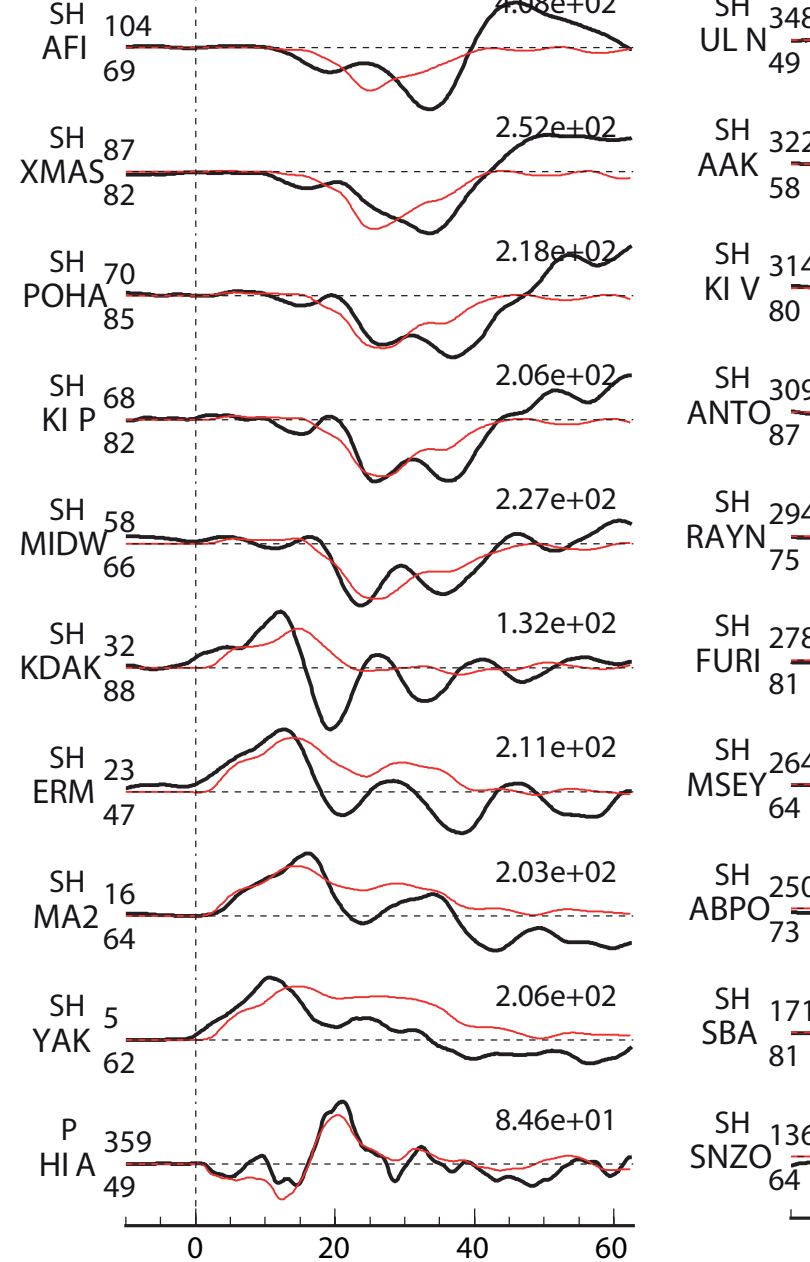
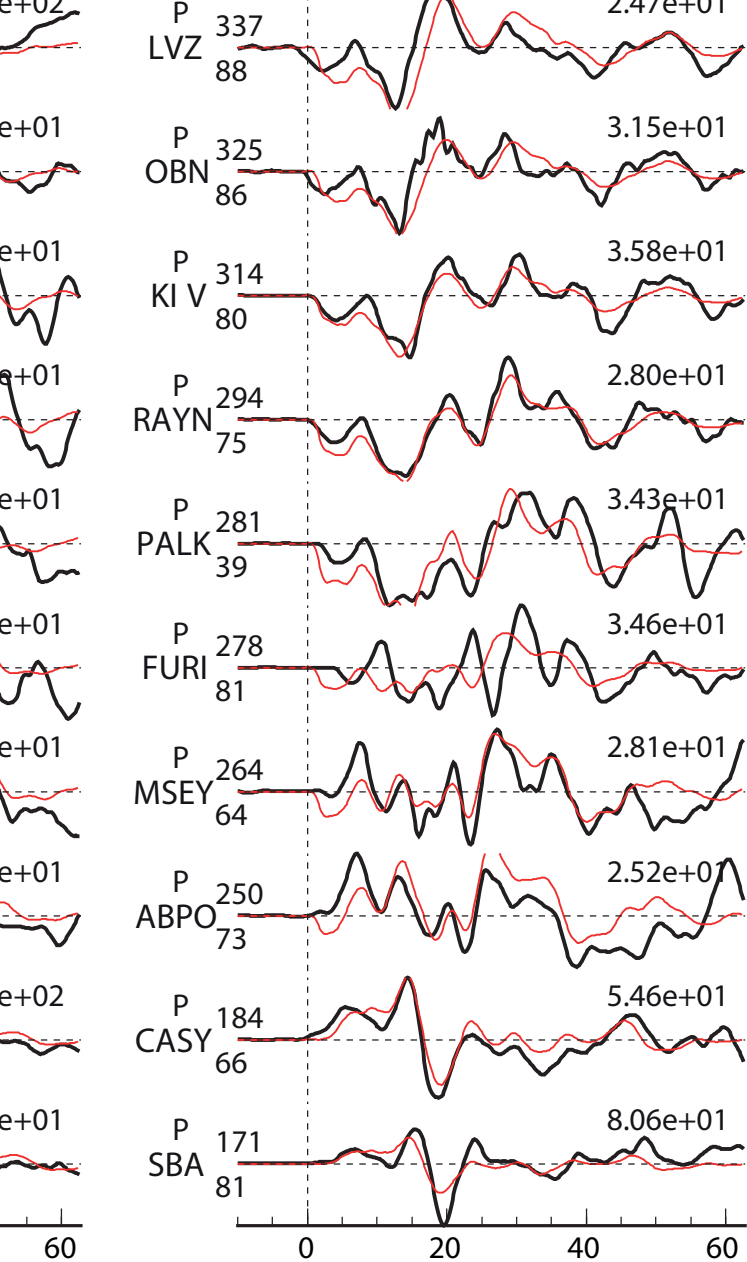
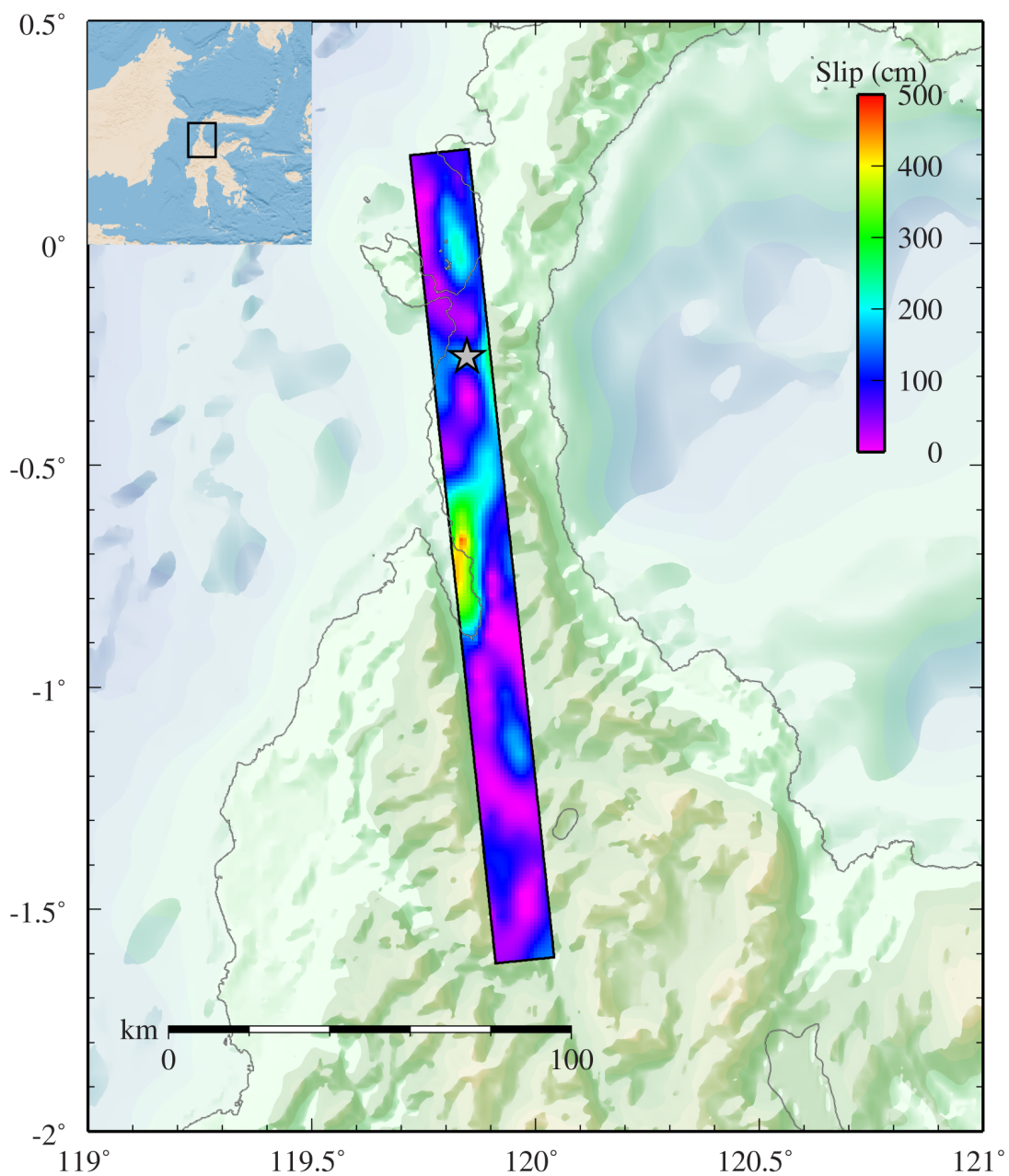


Figure 5.

(a)



(b)

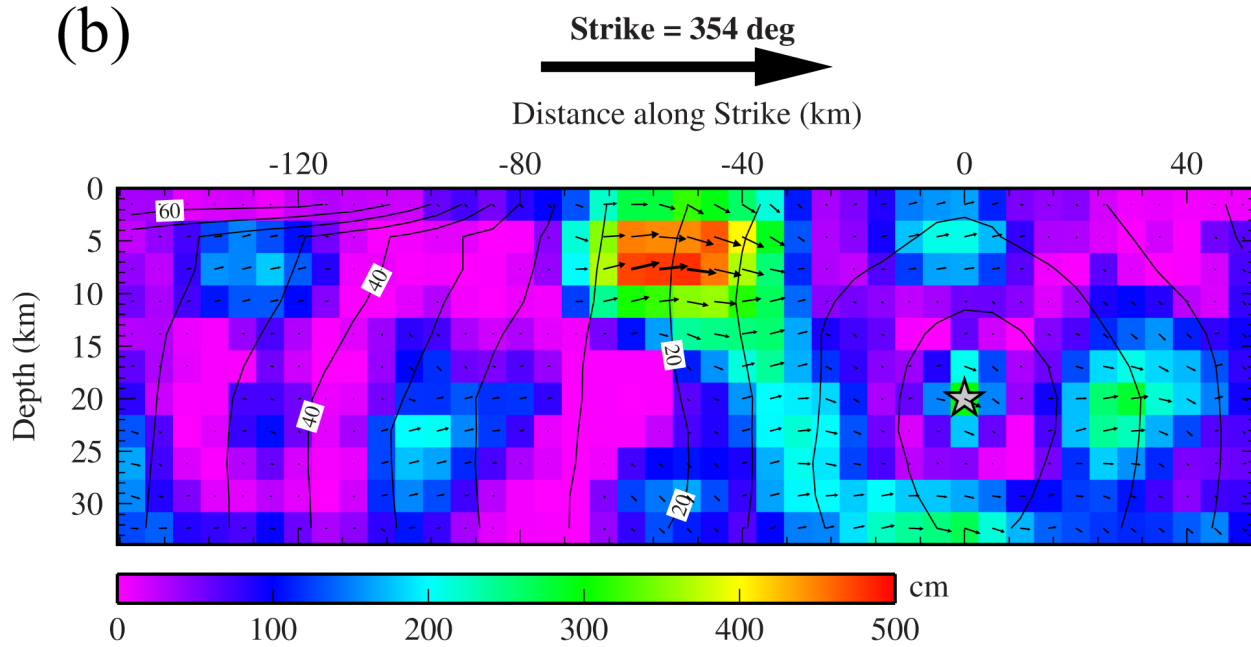
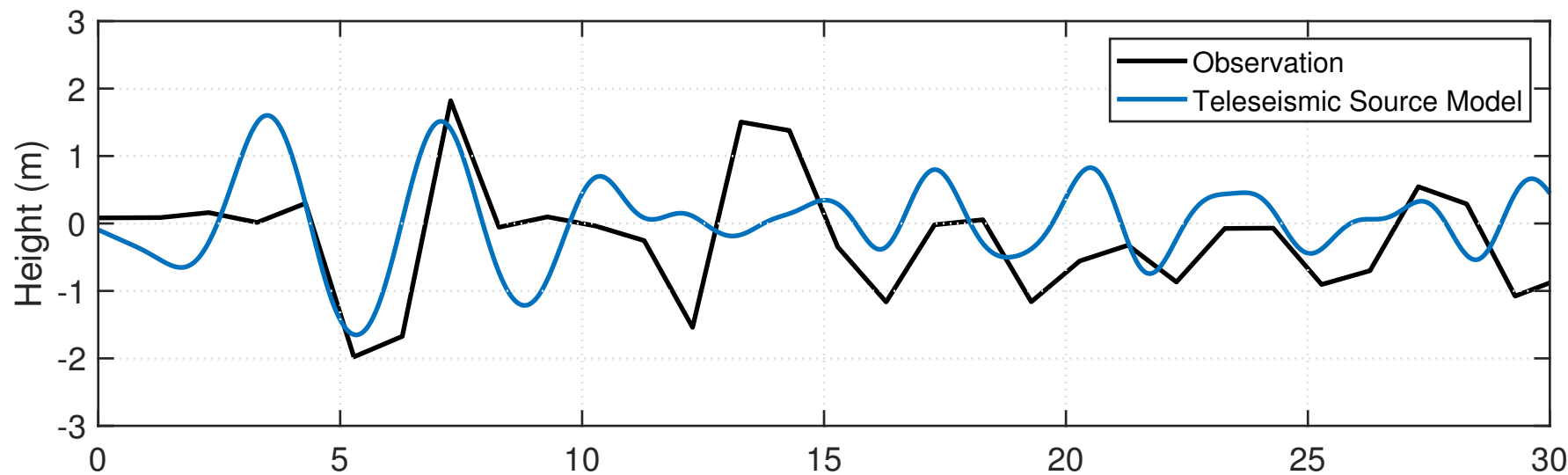


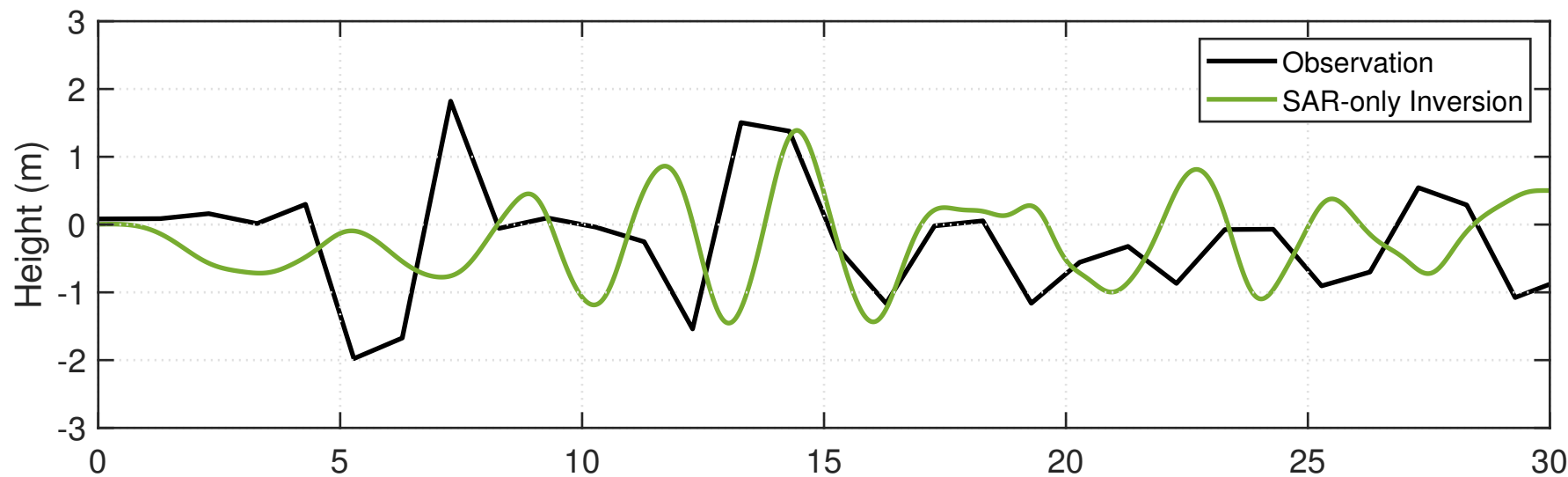
Figure 6.

Pantoloan

(a)



(b)



(c)

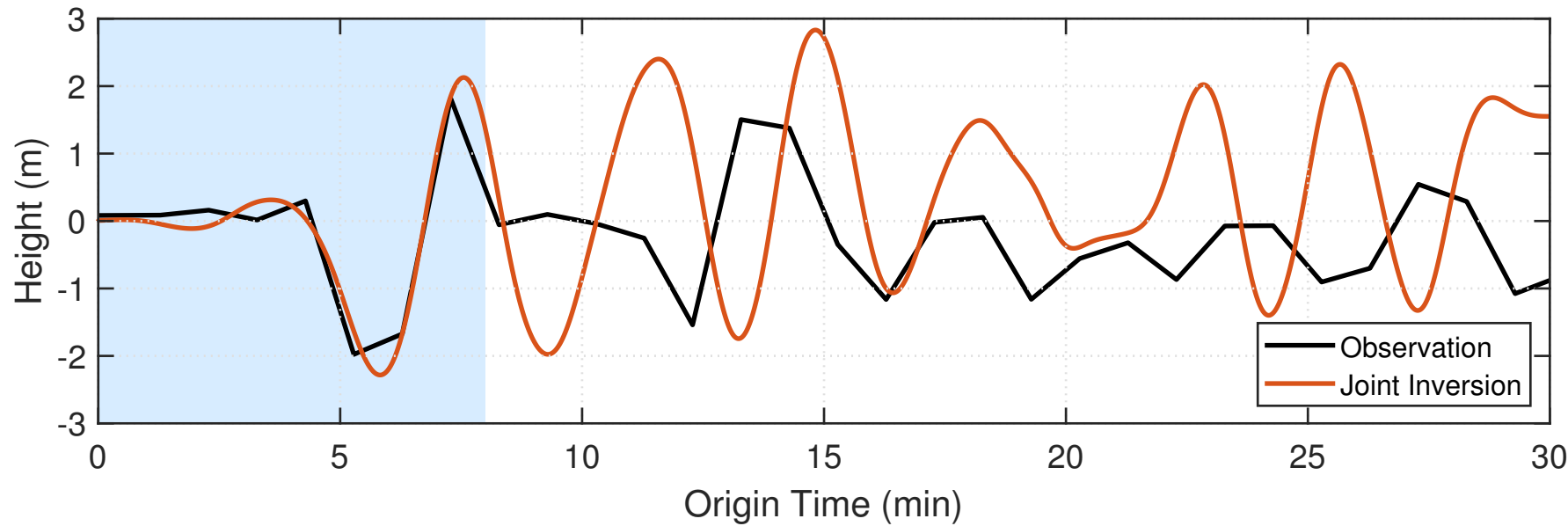
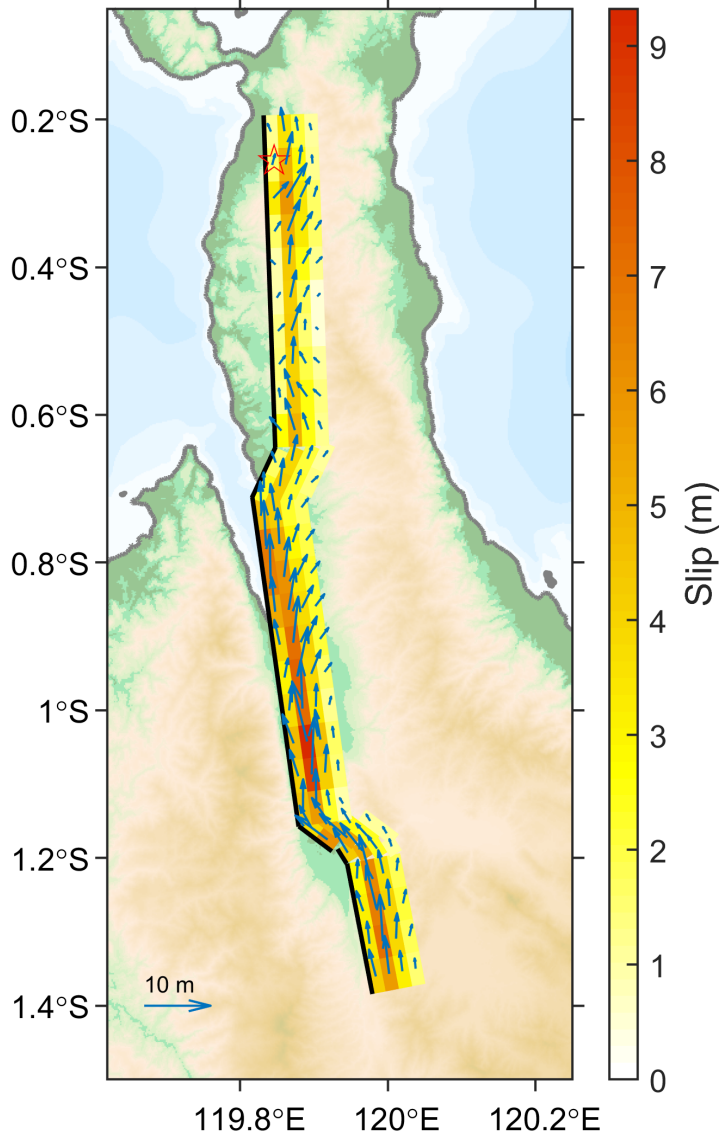


Figure 7.

(a)

SAR-only Inversion



(b)

Joint Inversion

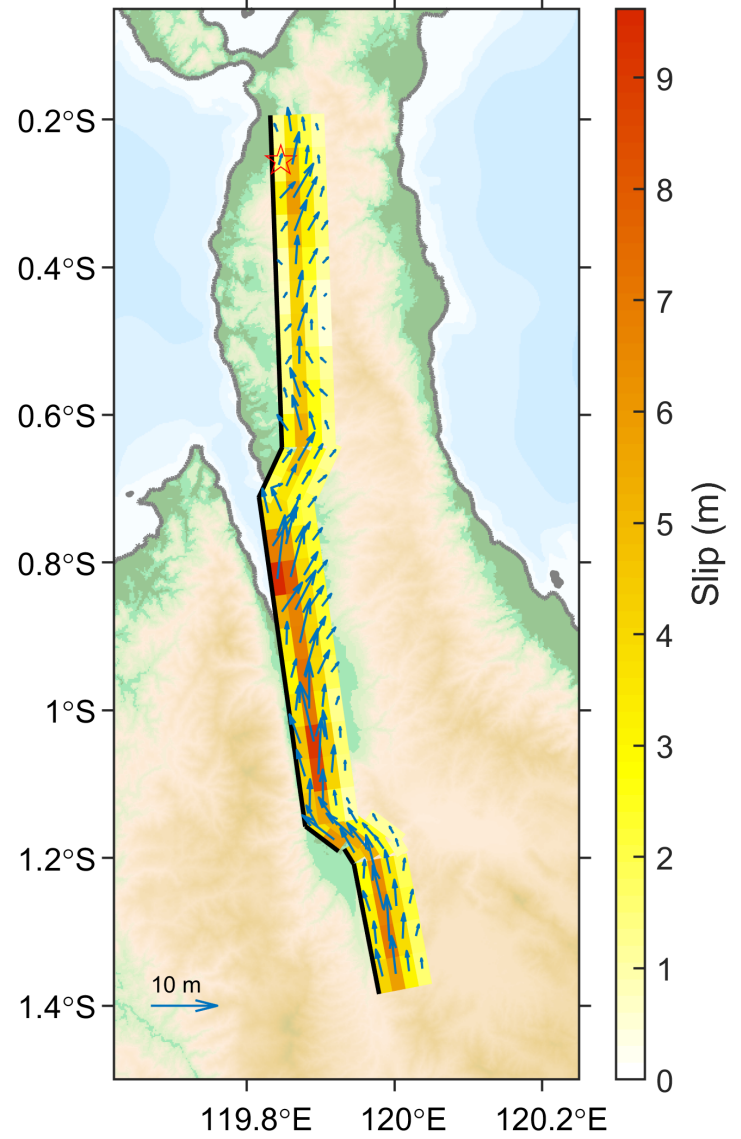
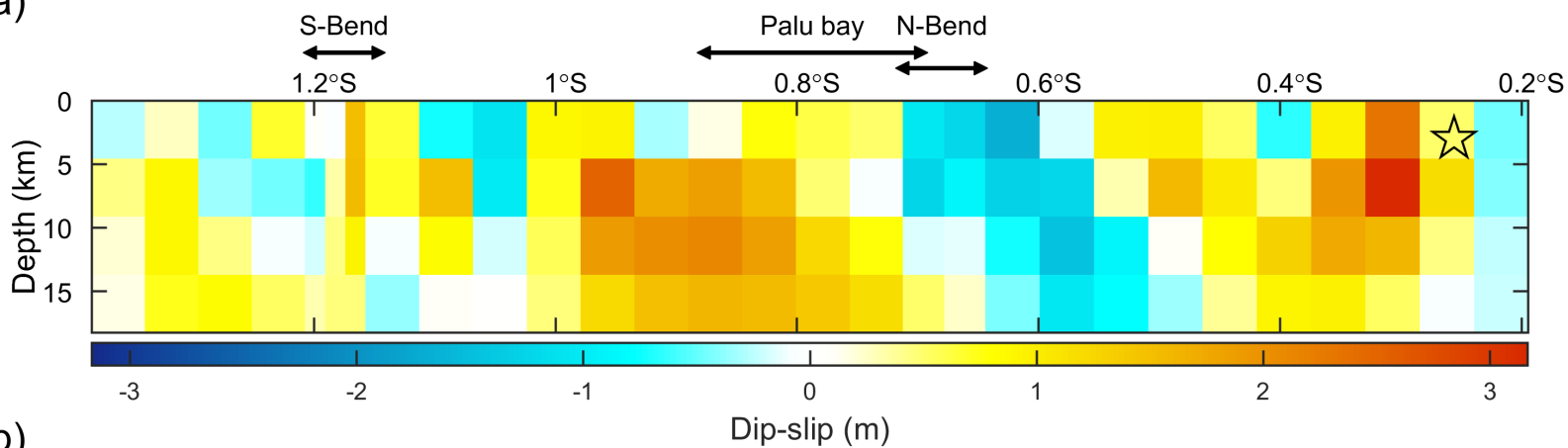
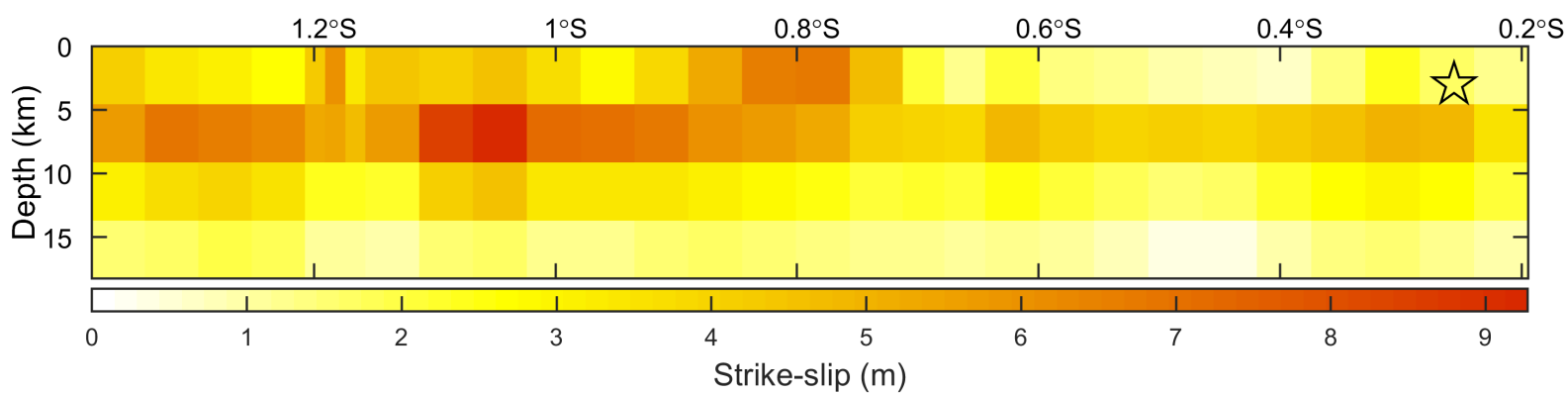


Figure 8.

(a)



(b)



(c)

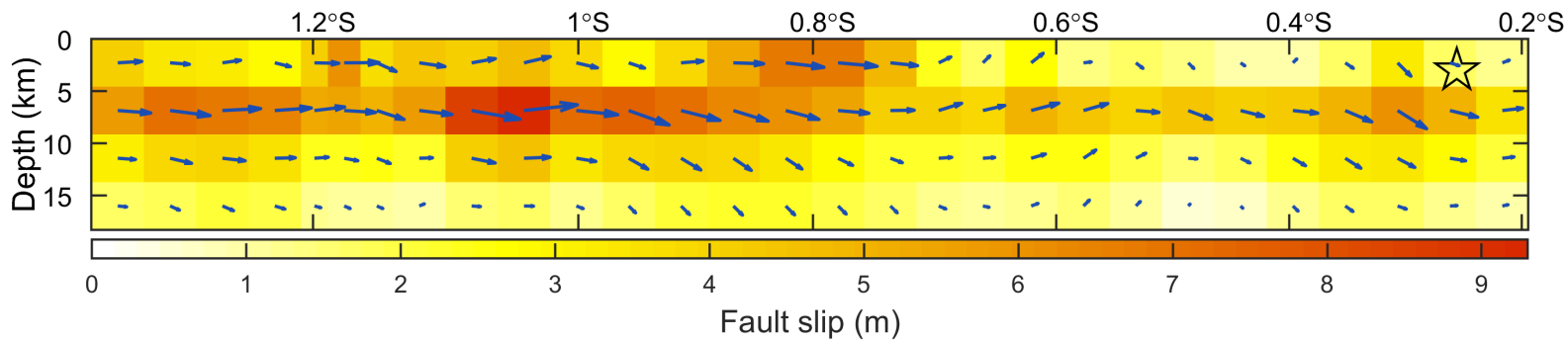
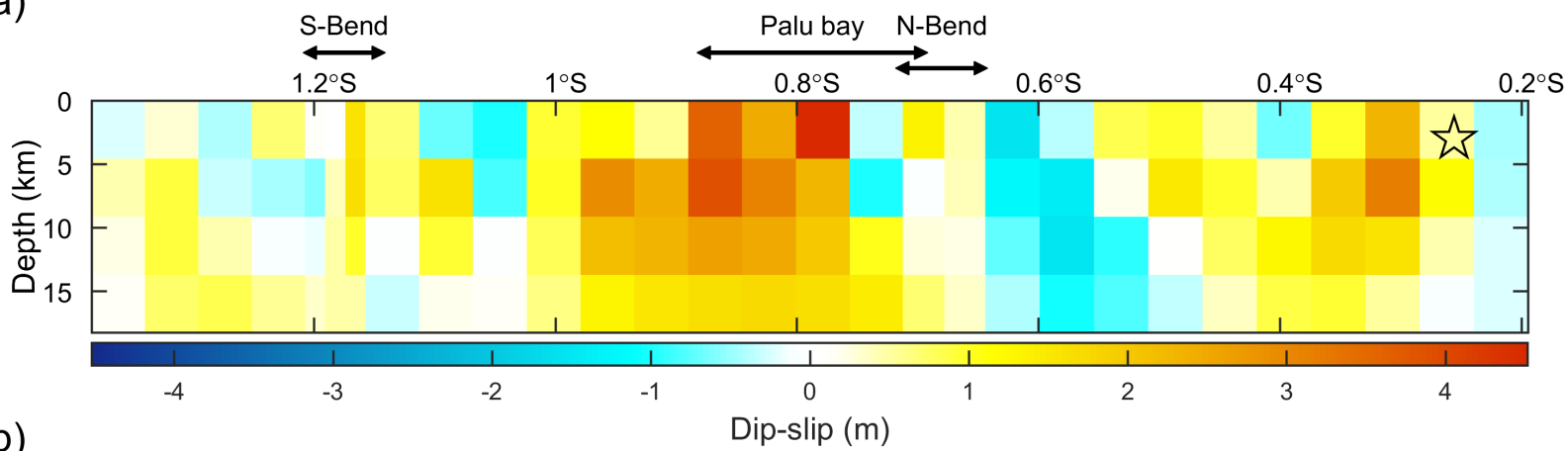
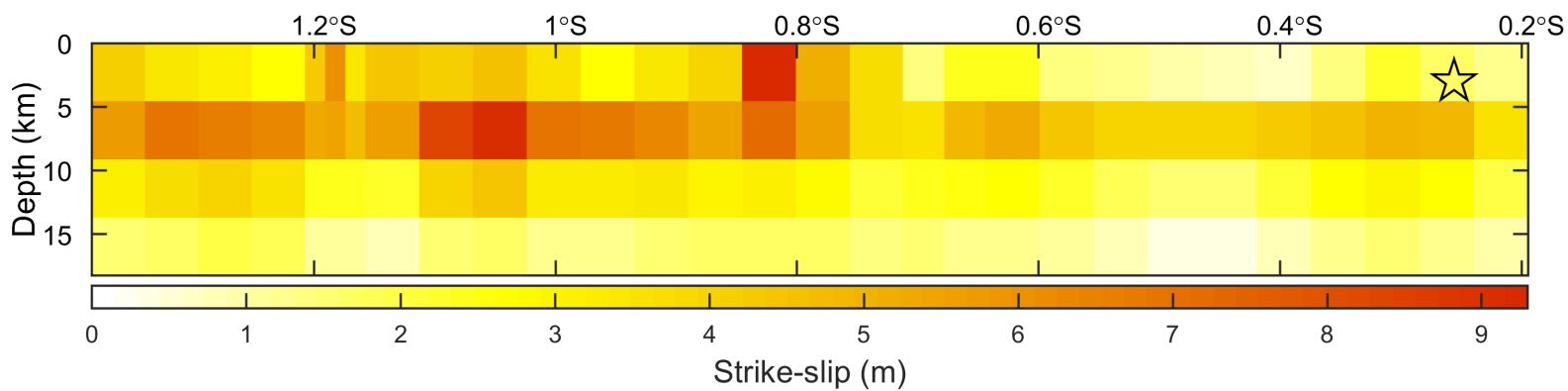


Figure 9.

(a)



(b)



(c)

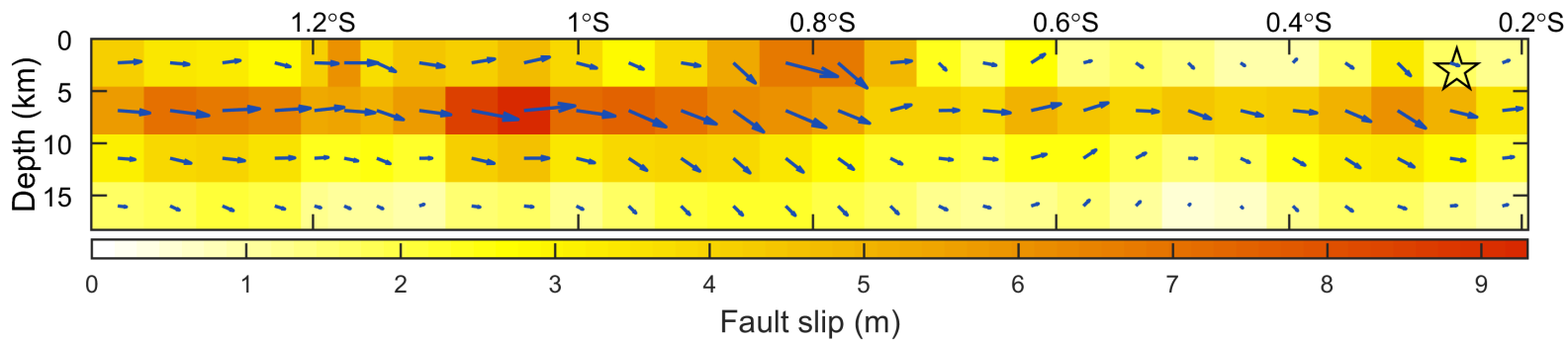
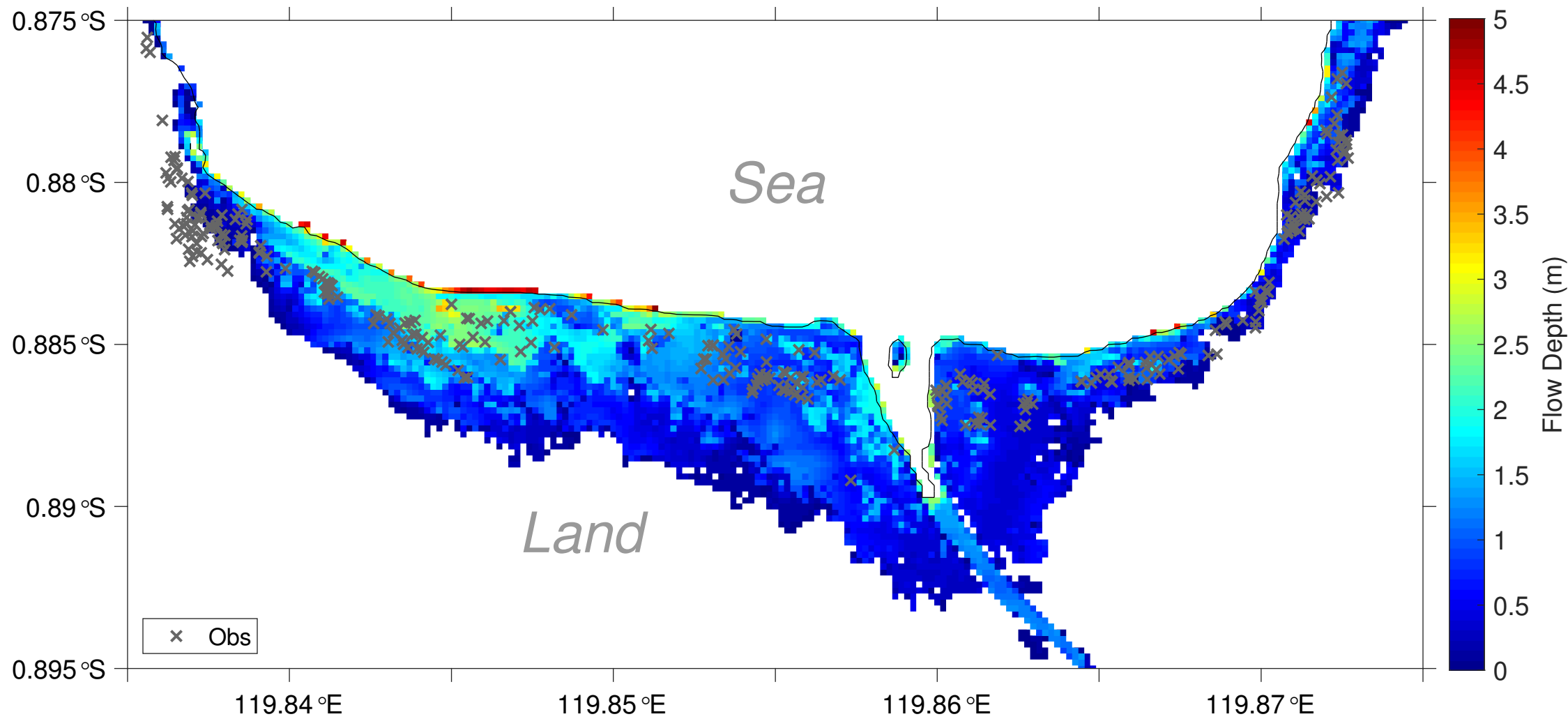


Figure 10.

(a)



(b)

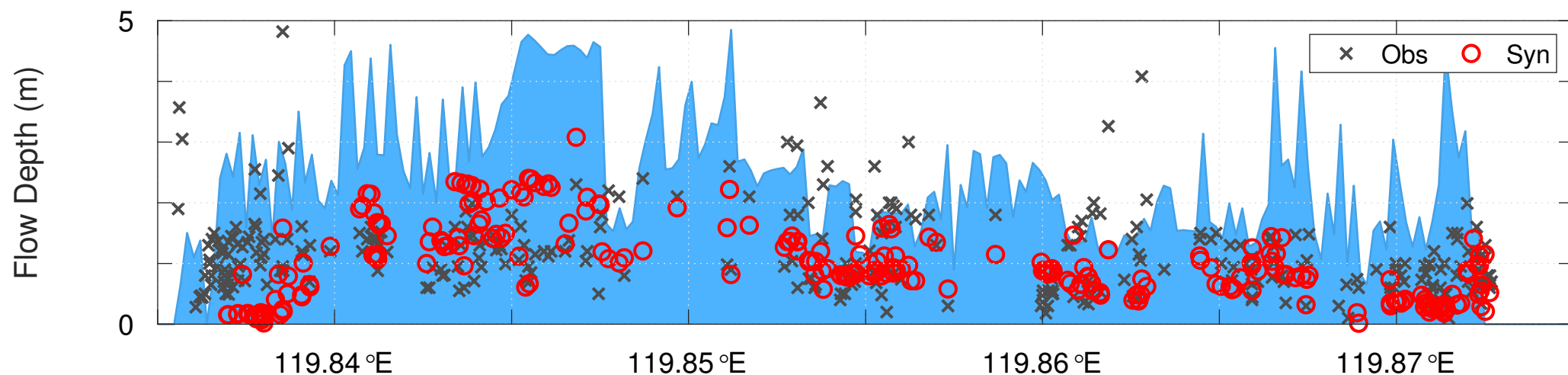
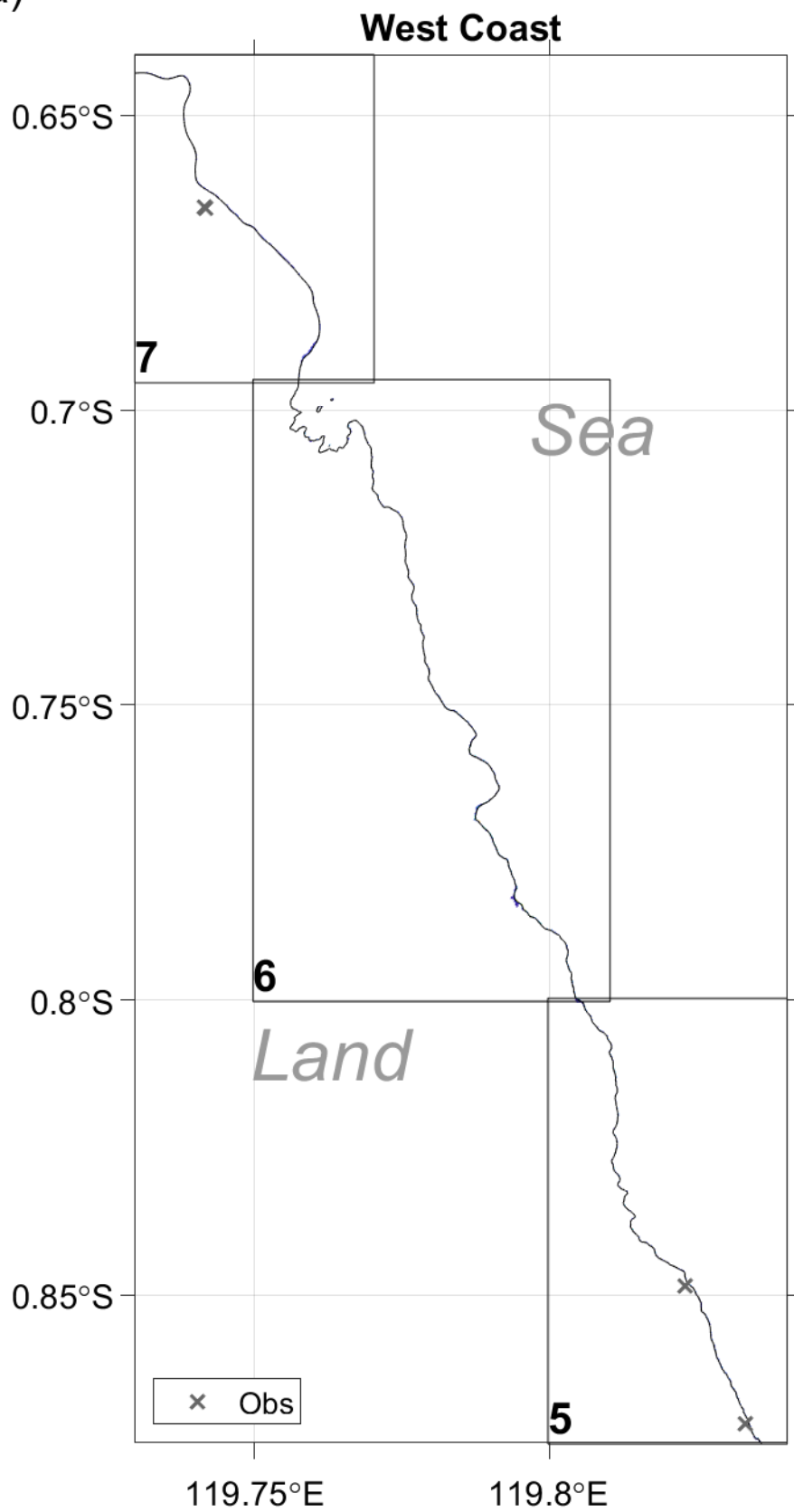


Figure 11.

(a)



(b)

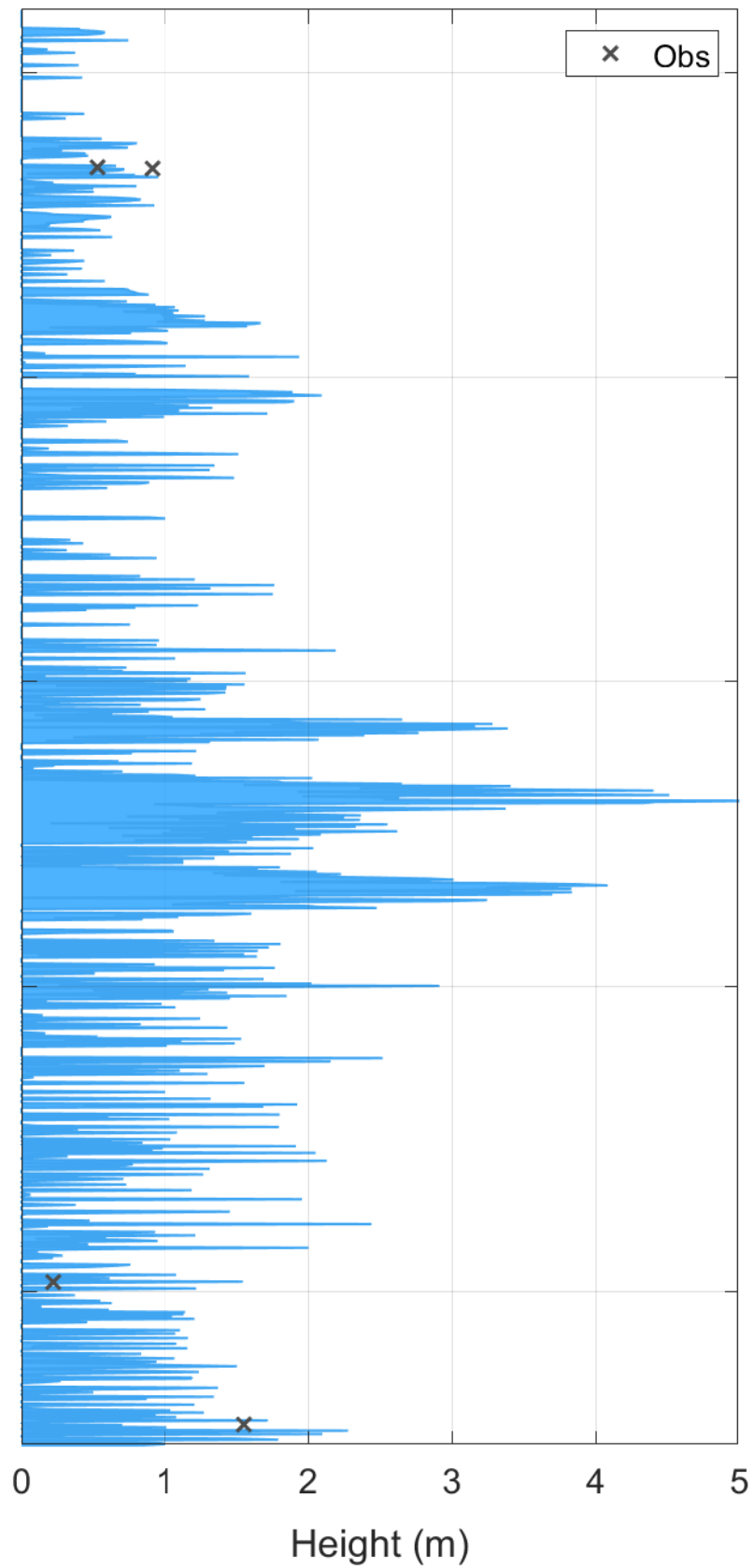


Figure 12.

